Simulation of Hydrogen Jet Exiting A High Pressure Reservoir

Mohammad Reza Kameshki

A Thesis

in

the Department

of

Mechanical and Industrial Engineering

Presented in Partial Fulfillment of the Requirements
for the Degree of Master of Applied Science (Mechanical Engineering) at
Concordia University
Montreal, Quebec, Canada

August 2007

Your file Votre référence
ISBN: 978-0-494-34629-7
Our file Notre référence
ISBN: 978-0-494-34629-7

ABSTARCT

SIMULATION OF HYDROGEN JET EXITING A HIGH PRESSURE RESERVOIR

Mohammad Reza KAMESHKI

Hydrogen release from a high pressure vessel is simulated using a computational fluid dynamic (CFD) code. An existing compressible Euler CFD solver is extended to solve the mixture of fluids together with extra transport equation for hydrogen species concentration. The modifications to the governing equations are presented as well as the discretization with the same techniques as the core solver. The core solver uses an implicit conservative scheme which is based on a finite volume technique for spatial discretization. The mixture of fluids is assumed to obey the ideal gas law and hence pressure, temperature, and density are coupled using the perfect gas equation of state. The code is used to simulate and study an inviscid hydrogen jet exiting a reservoir with initial pressures of 100 and 800 bars. The results obtained for the 100 bars test case are compared with the available data from another numerical simulation. Excellent agreement is observed.

ACKNOWLEDGMENTS

This research would not have been possible without the help of many people. Many thanks to my supervisor Dr. Marius Paraschivoiu for all his support; thanks to my colleagues and friends in the CFD lab especially Kaveh Mohamed for his very important suggestions throughout this project.

I dedicate this thesis to my dear parents, with all their love, support and encouragement, whom I owe all my identity to.

Table of Contents

LIST OF FIGURES

LIST OF TABLES

LIST OF SYMBOLS

Name	Definition
$\vec{V}$	Velocity vector
C_i	Concentration of species i
c_p	Constant pressure specific heat capacity
c_v	Constant volume specific heat capacity
D_C	Hydrogen-air binary mass diffusion coefficient
D_{ij}	Binary mass diffusion coefficient
D_{im}	Effective binary mass diffusion coefficient
E	Specific total energy
e	Specific internal energy
$\vec{g}$	Gravity acceleration vector
H	Specific total enthalpy
h	Specific internal enthalpy
$\bar{\bar{I}}$	5 by 5 unit matrix
k	Thermal conductivity constant
Le	Lewis number
M_i	Molecular weight of species i
p	Pressure
R_0	Global ideal gas constant
R_{gas}	Specific ideal gas constant
T	Temperature
t	Time
X_i	Species mole fraction
ρ	Density
$\vec{\nabla}$	Gradient vector operator
δ_{ij}	Kronecker delta
∂_j	Partial derivative operator
γ	Adiabatic index
μ	Dynamic viscosity coefficient
$\bar{\bar{\tau}}$	Stress tensor

1

Introduction

In this chapter,

an introduction to hydrogen release problems and its applications is presented. Then, the works previously done on this subject by other researchers is reviewed. This chapter finally ends with the goals that are set to be reached, a plan for achieving these targets, and the outline of the materials to be followed in this thesis.

1.1 Hydrogen: an alternative fuel

There is a widespread attempt to find clean and reliable energy substitutes because fossil fuels are responsible for the majority of the greenhouse gas emission, and also the fact that a significant part of the air pollutants is due to the combustion of the hydrocarbon fuels. The need for replacement of hydrocarbon fossil fuels becomes even more essential when considering the quickly diminishing natural reserves of fossil fuels. Hydrogen is one the promising ideal substitutes of the hydrocarbon-based fuels.

Hydrogen is carbon-free and a clean energy carrier in the foreseeable future. It is renewable and can be produced locally almost anywhere. If sustainable energy resources are used for hydrogen production, hydrogen will be a perfectly clean fuel with water or its vapor being the only by-product of its combustion. The importance of hydrogen role in future energy economy becomes more evident when considering the investment of different states across the globe on hydrogen infrastructure. For instance, the EU is advancing its hydrogen program through its European Hydrogen and Fuel Cell Technology Platform (HFP). In 2003 the US president announced a 1.2-billion dollars support to be spent over 5 years on hydrogen infrastructure research and development.

1.2 Hydrogen storage

One the issues associated with using hydrogen as a fuel is its storage. Although there are different methods of storing hydrogen the most probable solution in the short term is the storage of compressed hydrogen gas. However, compared to common hydrocarbon fuels, hydrogen has the smallest volumetric energy density, [1]. Table 1.1 shows a comparison of energy densities of different common fuels with hydrogen's energy density.

Fuel	Energy Densities
Hydrogen	270 Btu/ft3 (10,050 kJ/m3); gas at 1 atm and 60 ºF (15 ºC) 48,900 Btu/ft3 (1,825,000 kJ/m3); gas at 3,000 psig (200 barg) and 60 ºF (15 ºC) 121,000 Btu/ft3 (4,500,000 kJ/m3); gas at 10,000 psig (690 barg) and 60 ºF (15 ºC) 227,850 Btu/ft3 (8,491,000 kJ/m3); liquid
Methane	875 Btu/ft3 (32,560 kJ/m3); gas at 1 atm and 60 ºF (15 ºC) 184,100 Btu/ft3 (6,860,300 kJ/m3); gas at 3,000 psig (200 barg) and 60 ºF (15 ºC) 561,500 Btu/ft3 (20,920,400 kJ/m3); liquid
Propane	2,325 Btu/ft3 (86,670 kJ/m3); gas at 1 atm and 60 ºF (15 ºC) 630,400 Btu/ft3 (23,488,800 kJ/m3); liquid
Gasoline	836,000 Btu/ft3 (31,150,000 kJ/m3); liquid
Diesel	843,700 Btu/ft3 (31,435,800 kJ/m3) minimum; liquid
Methanol	424,100 Btu/ft3 (15,800,100 kJ/m3); liquid

Table 1.1 Energy densities of comparative fuels, [1].

In order to store enough hydrogen (for a range comparative to fossil fuels) in a vehicle, it has to be compressed at high pressures up to 800 bars. These high pressures along with hydrogen wide flammability range cause serious concerns on the use hydrogen as a fuel in public. Figure 1.1 shows the flammability range of hydrogen and common fossil fuels. As it is depicted in this diagram in case of a leakage hydrogen has the highest chance of burn compared to other fuels with same level concentration. Consequently, this has raised serious concerns on the use of hydrogen as a fuel in public.

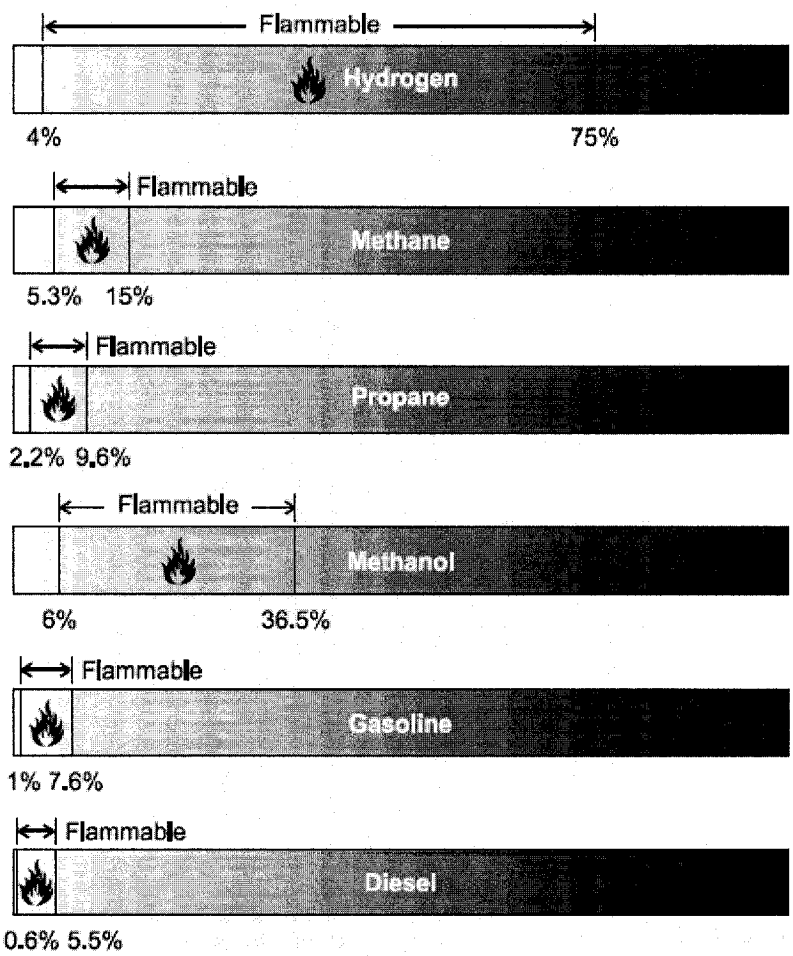

Figure 1.1 Hydrogen flammability range compared to common fuels at atmospheric temperature, [1].

In order to respond to these concerns, the hydrogen behavior and the formation of its cloud in a room in case of an accidental release from high pressure vessels, and the risks associated with such a phenomenon has to be studied. The results can then be used to build up safety standards for hydrogen mass-use by the public.

1.3 Objectives

Due to fundamental differences between hydrogen and other common fuels, in case of a leakage, hydrogen can reveal specific behaviors which have significant impacts on safety codes. Hydrogen flammability threshold, as mentioned in the previous section, is one of the important aspects of the release phenomenon which has to be determined before doing any risk assessment. The escaping hydrogen will mix with room air and produce a mixture. The flammability of this mixture depends on the local hydrogen mass fractions. The mixture will not burn if it is too lean or too rich. In order to predict consequences of hydrogen leakage it is necessary to know the temporal and spatial variations of hydrogen concentration in the mixture. From the other hand this requires a detailed knowledge flow pattern near the release area.

However, the process of hydrogen release from a high pressure vessel is accompanied with the formation of complex shock structures and interface surfaces. The shape and strength of these flow features depend on many factors such as stagnation pressure inside the tank, diameter of orifice, and the thermodynamical

properties of the ambient air as well as the room geometries. While steady jet has specified a large amount of research investigations by itself, still little knowledge is available about the details of the initial transient, particularly for large pressure ratios and strong shocks, stage of the release process, [33]. The purpose of this research is to study the effects of very high pressure ratios (the ratio of supply stagnation pressure to the ambient pressure) on the initial phases of the accidental release of hydrogen from a small orifice. An in-house Computational Fluid Dynamic (CFD) code is extended for numerical simulation of this problem. Although the operating pressures of the current pressurized vessels are in the range of 200-350 bars, potentially it may be up to 700 bars, [25], and in the literatures 1000 bars is also reported, [33]. Hence, we will simulate the hydrogen release from an 800-bar vessel from a 5mm-daimeter opening.

1.4 Review of previous works

Compressible high-speed jet of gas is of significant interest in many research fields. It is also observed in numerous practical engineering applications which can range from material processing, and laser machining, to rocket propulsion and combustion. Another example of these applications, which is also the subject of this thesis, is the accidental release of combustible high-pressure gases (hydrogen in our case) into the atmosphere. When a high-pressure gas is exhausted into through an orifice into a low-pressure chamber, the gas rapidly expands and results in formation of an underexpanded jet, [27].

Investigation of underexpanded compressible jets is reported in several numerical and experimental studies. While in the past the numerical techniques were limited due to lack of computational resources, the early experimental methods were also restricted to schlieren photography for qualitative analysis of the shock structure patterns and pressure probe measurements for global quantities such as Mach disk, [2,3]. Although more recently laser droplet anemometry and laser induced fluorescence have been used, the lag biasing of the seeding particles to the rapid changes of velocities across waves has limited the reliable data to the constant-pressure region of the flow, [4,5].

Among the earliest researches on highly underexpanded jet is the work by Adamson et al., [6], who presented an analytical method for calculating the position of the first normal shock, or Mach disk, in the behind a highly underexpanded nozzle. Their method gives good results compared to experimental photographs for pressure ratio in range of 5 to 140. An approximate method is also developed by Gostinstsev et al. [7], based on formulas of spiral isentropic flow for the location of Mach disk in the swirling flow downstream of nozzle without a diffuser section. They have argued that their method is also applicable to studying of non-swirling jet. The effect of orifice diameter on underexpanded jets is studied by Birch et al., [8], through an experimental investigation of flame stability in the natural gas jet. Emel 'yanov et al., [9], analyzed a large number of experimental data on the motion of the starting discontinuities along the axis to obtain relationships describing their dynamics over a broad range of the governing

parameters. The effects of temperature ratio and physical properties of outgoing flow and the ambient gases are studied by Golub, [10], who performed an experiment on the formation of unsteady jets using schlieren method. He has founded out that the ratio of outgoing gas temperature to the ambient gas strongly affects the transverse extension of the jet.

The near field shock structures of dual co-axial jets are studied by Rao et al., [11]. They performed an experiment using shclieren technique and studied the effect of outer nozzle on inner nozzle shock structures. Ishii et al., [12], have studied unsteady circular pulse jets both numerically and experimentally. They investigated different jet strengths and particularly focused on the formation of Mach disks and shock-cell structures during the evolution of the jet. Their numerical method was based on a TVD finite volume method for Euler system of equations. Devaud et al., [13], also studied the stability of underexpanded jet flames both numerically and experimentally. They examined the jet of H_2-CO mixture and the effect of adding CO to H_2 on flame stability.

Rahimi et al., [14], have experimentally studied the heat transfer between a highly underexpanded jet and a cylinder when the jet of gas impinges onto the heated surface of the cylinder. They studied the effects of underexpanded jet on cooling rate when the cylinder is placed at different location along the jet axis relative to the nozzle. The interactions between shock-cell structure and the large-scale vortices in the mixing layer downstream of an unsteady underexpanded jet create some acoustic noises which can

propagate across the mixing layer. Suzuki et al., [15], have studied this phenomenon in an underexpanded supersonic jet using direct numerical simulation (DNS) in two dimensions. Li et al., [16], have compared the performance of characteristic method and Fluent commercial CFD code to study the high pressure gas flow from a sonic nozzle. Although their CFD results were in good agreement with the corresponding results from characteristic method it should be kept in mind that since the Fluent is using the primitive variables instead of conservative variables the location of shocks predicted by Fluent may not be accurate. Another application of underexpanded gas jet is studied by Belan et al., [17], who conducted experiments by means of intense lasers to investigate astrophysical jets such as Herbig-Haro jets and the interaction between large-scale vortices and system of shocks. They have studied a number of orifice jets with the pressure ratio of the order 10^3-10^4. They also used a CFD code and compared their experimental results with those obtained from the CFD method. Due to technical difficulties in measurements in the region very close to the nozzle they only compared the experimental results with numerical simulations for the region downstream the Mach disk and observed good agreement between two sets of results.

The papers reviewed so far were mainly focused on region very close to the jet nozzle. However the complete investigation of the release process requires a larger physical domain of the flow. Nevertheless, the very high pressure of the stored hydrogen along with the small release opening (5 mm, for instance), sonic jet at the release point, and nearly zero velocity just a few meters after the jet make this problem

extremely difficult to compute. The first issue that arises when dealing with such a problem is the size of the mesh required to capture all features of the flow field. Due to the very fine mesh needed to simulate the 3D sonic release of hydrogen it demands a computational power which can even exceed the threshold of today's practically available supercomputers. This had led researchers to work on larger orifice sizes or lower pressure release scenarios. Sand et al., [18], has studied the release of natural gas from high-pressure pipelines due to a break in the pipe. They assumed the natural gas to be real gas using a generalized equation of state and simulated the flow and dispersion of gas using a CFD finite volume code. The release area they modeled is the entire 0.7m--cross section of the pipe which means they assumed that the break causes the pipe to completely split in two parts. In order to avoid calculation of the high pressure gradient at the pipeline break point they modeled the underexpanded flow on subgrid level using simplified conservation equations in integral form to compute approximately the equivalent nozzle area corresponding to the exit area of the shock structure. For the turbulence modeling they applied the Reichard and k-ε models for pipe and dispersion field respectively.

Breitung et al. [19] have numerically simulated the release of hydrogen from a 10×20-cm^2 opening in a private 2.4×4.5×6.5-m garage. The speed of release through a relatively large orifice is subsonic set by a constant mass flow rate with a specified duration. They have used two different structured meshes with approximately 70000 and 111000 cells. Venetsanos et al. [20] have done one of the most comprehensive

studies on hydrogen release. They simulated the 1983 Stockholm hydrogen accident in which hydrogen was discharged from a rack of 18 inter-connected 200-bar hydrogen vessels into an urban environment. The accident happened due to failure of 6-mm diameter connecting pipes. However, the entire release and combustion process is modeled by using three different CFD codes due to differences in physics and scales between the different phenomena. Nevertheless, their codes employ dynamically adapted grids with mesh nodes varying from 26000 to 300000 during different stages of the simulations. The two-equation k-ε model is used for turbulence modeling while the mixture is assumed to be an ideal gas.

Agranat et al. [21] simulated a sonic release of hydrogen from a 0.25-in opening in a simple 3D geometries, however, little information is obtained about the complex shock structures near the release point. Angers et al. [22] have simulated the subsonic release of hydrogen from a 10-mm diameter into a 3D room configuration. They applied the RNG k-ε model for turbulence modeling. Wilkening et al. [23] have modeled the 2D release of hydrogen from a 20-cm wide opening through an 11-bar pipeline using ideal gas assumption. Mukai et al. [24] modeled the hydrogen subsonic release from a 5-cm hole in tunnels and underground parking lots. They also used k-ε turbulence model. Pedro et al. [25] have studied a round jet of hydrogen releases from a 100-bar pressure vessel into hydrogen. They applied mesh adaptation and focused on the initial transient jet which exits from a 5-mm orifice.

Another important issue in simulation of hydrogen release is the real gas behavior of hydrogen at the release point. As verified by Mohamed et al. [26] hydrogen release properties based on ideal gas assumption from a high pressure chamber are different from the results obtained assuming real gas.

1.5 Thesis outline

As previously mentioned, the purpose of this research is to develop a CFD tool for studying of hydrogen release from high-pressure vessels. Although some codes currently exist and are used for the simulation of this flow, the accuracy of these codes in prediction of flow field parameters is not well known. For instance, as discussed earlier in the literature review section, Fluent commercial code is based on primitive variable instead of conservative variables. This in fact can lead to inaccurate prediction of shocks locations. In addition the maximum pressure ratio that is modeled by Fluent, as far as the author has seen in the reviewed literatures, is 100 which is far less than the practical application pressure ratios. Hence in order to be able to accurately simulate hydrogen release phenomenon with pressure ratio of up to 800 bars an existing in-house compressible CFD code will be extended to solve the mixture of fluids and also to solve an extra transport equation for the hydrogen species conservation. The code is based on a finite volume conservative scheme for numerical discretization. In chapter 2 modifications to the governing equations are presented and numerical discretization is described. First the Euler set of equations are presented for the mixture of fluids. The

species transport equation is then presented and discretized using the same numerical scheme as the main core solver. The numerical results obtained are then presented in chapter 3 and compared with available similar results. In chapter 4 some conclusions are made based on the results presented in chapter 3 and some future works are suggested.

2

Governing Equations and Numerical Techniques

In this chapter,

the physical problem and equations governing the flow of fluid mixtures are introduced. Also the non-dimensionalization parameters are mentioned. The numerical schemes used for the space and time discretization of the governing equations are then described. This chapter ends with the method used for the numerical flux calculations.

2.1 Highly underexpanded jet flow

Underexpanded jets form when a gas flows from a high-pressure vessel into a low pressure chamber through an orifice. Due to pressure mismatch at the exit of the nozzle after release of high pressure gas an expansion fan originating at the corners of orifice is generated. Figure 2.1 represent a schematic of shock waves structure formed in a slightly underexpanded jet. The expansion waves later are reflected at the jet boundary as compression waves so that the jet boundary pressure remains the same as the ambient pressure, [16]. At higher pressure ratios the reflected compression waves come together into intercepting shocks which meet at the symmetry axis and form the diamond-shape shock cells.

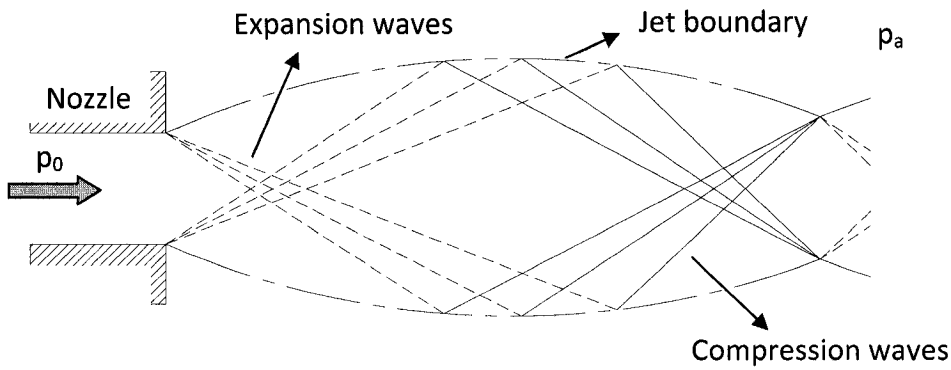

Figure 2.1 Shock waves structure in slightly underexpanded jet, $p_0 > p_a$

At relatively low-pressure ratio the reflected compression waves of the underexpanded jets will not merge together at the jet axis to form the diamond cells. Instead they periodically expand and re-converge as the jet boundary oscillates in an

effort to match the ambient pressure. The gas cools as it flows through rarefaction fans and heats when it passes through the shock diamonds. At very high-pressure ratios the intercepting shocks can no longer reflect at the centerline and instead they conflate to form the barrel shock that terminates in a triple-point as shown in schematic diagram of Figure 2.2, [16,27].

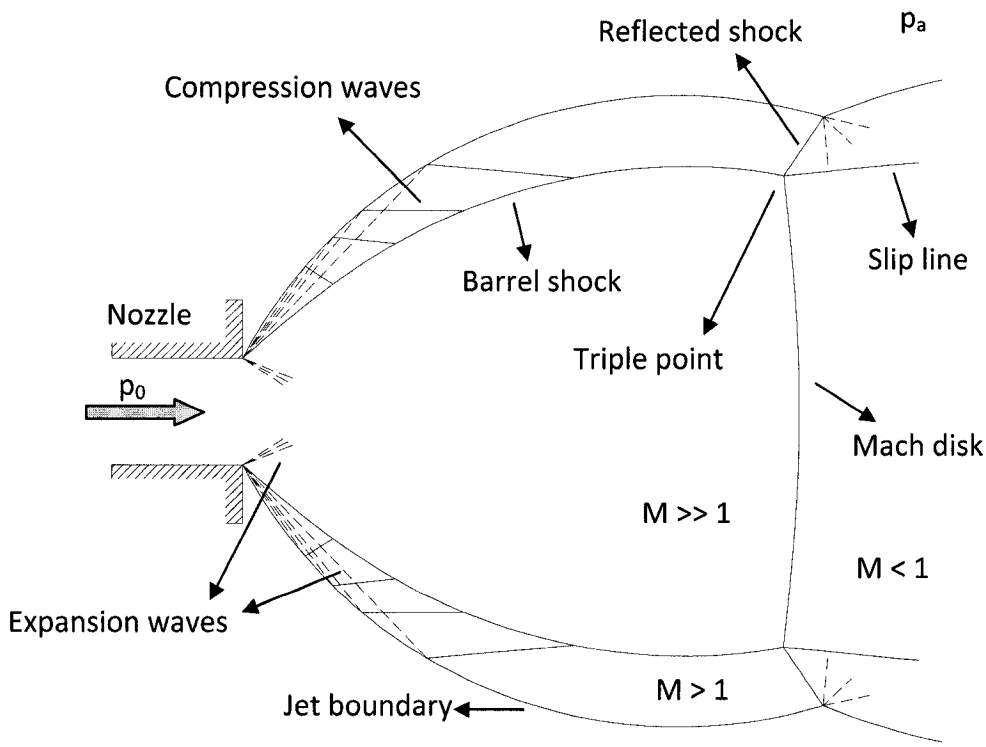

Figure 2.2 Highly underexpanded jet shock structures, $p_0 >> p_a$

The key features of highly underexpanded jet include the barrel shock, jet boundary, triple point, Mach disk, and the reflected shock. The Mach disk is a slightly curved shock behind which there is a large region of subsonic flow bounded by the slip line emanating from the triple point. While the flow inside the shock barrel is highly supersonic the flow

across the barrel shock remains supersonic too but with Mach numbers lower than the core of the jet.

2.2 Euler equations for highly underexpanded jets

Due to high Reynolds number (11×10^{-6} in present study based on the orifice diameter) in highly underexpanded jets in the region close to the nozzle the convective velocities dominate the diffusive velocities except at very thin layers around shocks and contact surfaces where sharp gradients exist, [38]. Experimental investigations by many researchers, [28,29,30], and numerical results, [4,31], have confirmed that the flow is inviscid in the near-field shock-containing region of supersonic jets. In addition, Ho et al., [32], and Grinstein et al., [33], have shown that the basic vortex dynamics in a shear layer is essentially inviscid. These features of supersonic jets allow us to model the highly underexpanded jets using compressible Euler[1] equations.

2.2.1 Euler equations for a gas mixture

In the absence of chemical reactions or any other mass exchange mechanism the mass of each species is conserved so that each species obeys a continuity equation of the same form as the continuity equation for a pure fluid, [34].

[1] The Navier-Stokes extension of the governing equations of the flow is also completed as part of my Master's thesis, however due to the study of the jet close to the nozzle, only inviscid results are presented. Interested reader can find the Navier-Stokes formulation in the appendix section.

$$\frac{\partial \rho_i}{\partial t} + \vec{\nabla} \cdot (\rho_i \vec{V}_i) = 0 \qquad 2.1$$

Where $\vec{V}_i$ is the velocity of species i. Summation of conservation equations of the mixture species yields the continuity equation for the mixture.

$$\frac{\partial \rho}{\partial t} + \vec{\nabla} \cdot (\rho \vec{V}) = 0 \qquad 2.2$$

The velocity in the above equation is the mass-averaged velocity of the mixture species defined below:

$$\vec{V} = \sum_i C_i \vec{V}_i \,. \qquad 2.3$$

In the above equation C_i is the local mass fraction of species i and is defined as follows.

$$C_i = \frac{\rho_i}{\rho} = \frac{m_i}{m}, \qquad 2.4$$

where ρ_i is the partial density or concentration of species i. The following relationships can also be deduced from the above formulations.

$$\rho = \sum_i \rho_i \qquad 2.5$$

$$\sum_i C_i = 1 \qquad 2.6$$

Defining the other mixture properties in terms of mass-averaged quantities, the momentum and energy conservation equation can be constructed in the same manner as for the mass conservation equation for the gas mixture, [34,35,36].

$$\frac{\partial(\rho\vec{V})}{\partial t} + \vec{\nabla}\cdot(\rho\vec{V}\otimes\vec{V} + p\bar{\bar{I}}) = \rho\vec{g} \qquad 2.7$$

$$\frac{\partial(\rho E)}{\partial t} + \vec{\nabla}\cdot(\rho\vec{V}H) = \rho\vec{g}\cdot\vec{V} \qquad 2.8$$

with,

$$H = h + \tfrac{1}{2}V^2 \qquad 2.9$$

$$h = e + p/\rho \qquad 2.10$$

$$E = e + \tfrac{1}{2}V^2 \qquad 2.11$$

2.2.2 Equation of state

Three levels of approximation can be defined in terms of equation of state (EOS), purely ideal gas, partially ideal gas, and real gas assumptions which are described below.

- **Purely ideal gas**

Under this assumption we ignore the variation of the adiabatic index due to pressure or temperature changes. The only source of variation which can affect γ is the change in

species local mass fraction. Based on this argument, for a pure ideal gas, we can write the following relationships.

$$c_p = \sum_i c_{p_i} c_i \qquad 2.12$$

$$c_v = \sum_i c_{v_i} c_i \qquad 2.13$$

$$\gamma = c_p / c_v \qquad 2.14$$

However, since the γ for hydrogen and air is almost the same (1.41 and 1.4), we ignore the variation of γ. Finally for the EOS we can write:

$$p = \rho R_{gas} T \qquad 2.15$$

$$R_{gas} = R_0 \sum_{i=1}^{2} \frac{C_i}{M_i} \qquad 2.16$$

$$e = c_v T \qquad 2.17$$

$$h = c_p T \qquad 2.18$$

$$p = \rho(\gamma - 1)e \qquad 2.19$$

- **Partially ideal gas assumption**

At this level of approximation we consider the variation of the adiabatic index with pressure or temperature, but yet it is assumed that the whole mixture behaves like an

ideal gas. Based on the ideal gas assumption that c_p and c_v are only functions of temperature and we can calculate them from the following formula:

$$C_{pi} = a_0 + a_1 T + a_2 T^2 + a_3 T^3 + a_4 T^4 \qquad 2.20$$

The order of the above polynomial can be chosen according to the desired accuracy level of the problem and can be considered to be linear. As it is clear from the above equation, although the temperature is the same for all species, the polynomial coefficients can be different for different mixture components. At the end we can determine γ as follows:

$$\gamma = \frac{h}{e} \qquad 2.21$$

Here the equation of state remains the same as in the previous case.

- **Real gas assumption**

In this case all of the parameters may depend upon the specific real gas model which is used.

In order to avoid any complexity at this stage of the research, the mixture of hydrogen and air is assumed to be a pure ideal gas. In addition, the flow, as previously mentioned, is considered to be non-reactive and also adiabatic.

2.2.3 Species conservation equation

In the abovementioned Euler equations for gas mixture there are seven unknowns and six equations, hence another relationship is required to close this system of equations. This equation is the species conservation equation through which transportation of mixture component is modeled.

$$\frac{\partial(\rho C_a)}{\partial t} + \vec{\nabla} \cdot (\rho C_a \vec{V}) = 0 \qquad 2.22$$

In order to minimize the numerical error, the above equation is written for the major component of the mixture which in the present case is the air mass fraction C_a. Hydrogen mass fraction then can be easily determined from equation 2.6. It should be mentioned that due to inviscid assumption for the gas mixture the diffusion term[2] is also neglected in equation 2.22.

2.2.4 Non-dimensionalization

The following parameters are used in order to non-dimensionalize the system of the governing equations. In these definitions the parameters with the plus sign indicates the non-dimensional quantity.

$$x = L_0 x^+ \qquad \rho = \rho_0 \rho^+ \qquad c_p = c_{p0} c_p^+$$
$$u = u_0 u^+ \qquad p = \rho_0 u_0^2 p^+ \qquad g = (u_0^2 / L_0) g^+$$
$$t = (L_0 / u_0) t^+ \qquad R_{gas} = c_{p0} R_{gas}^+ \qquad \rho_a = \rho_0 \rho_a^+$$

[2] Interested readers can find the diffusive version of this equation in the appendix section.

2.3 Numerical techniques

The numerical methods which are used in this research are based on an implicit mixed finite element-finite volume scheme, [37]. According to this scheme, finite element technique is used for all diffusive and source terms, while for temporal and convective terms finite volume integration is applied. Figure 2.3 shows a two dimensional schematics of finite elements and finite volumes used in numerical integration of the governing equations.

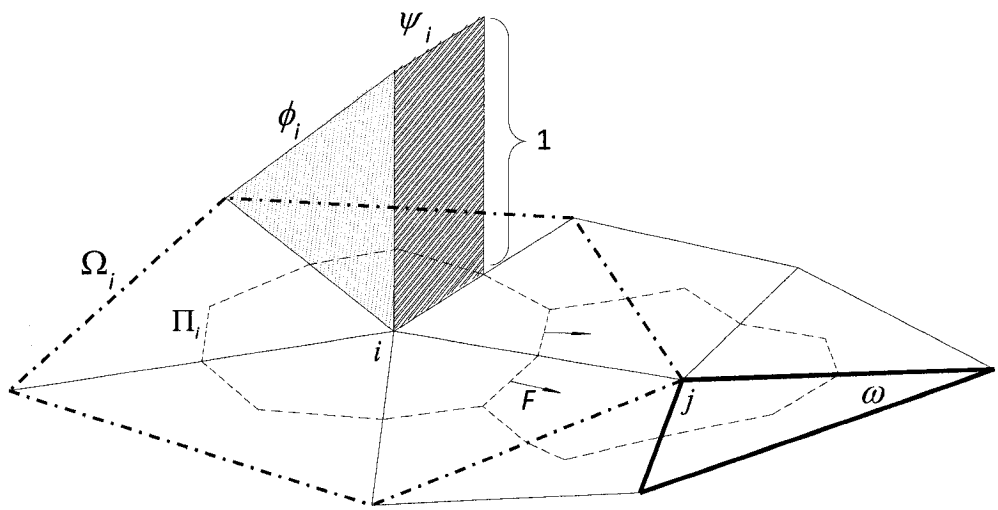

Figure 2.3 Two dimensional representation of finite volumes and control volumes

The parameters used in Figure 2.1 are defined as follow:

ω ≡ Finite elemnet tetrahedrds
Π_i ≡ Finite volume surrounding node*i*
Ω_i ≡ Community of finite elements surrounding node*i*
ϕ_i ≡ Finite element shape function
ψ_i ≡ Finite volume shape function

As it is shown in Figure 2.3 different shape functions are used for finite elements and finite volumes. For finite elements the shape function linearly varies from one at node *i* to zero at the element boundaries, while for finite volumes the shape is one all over the control volume and zero everywhere else.

2.3.1 Discretization of the species transport equation

In order to discretize the species transport equation a weak formulation is written as follows:

$$\int_{\Omega} \frac{\partial(\rho C_a)}{\partial t} \psi \, d\sigma + \int_{\Omega} \vec{\nabla} \cdot (\rho C_a \vec{V}) \psi d\sigma = 0 \qquad 2.23$$

Where, ψ is the test function and is the same as shape function. Using the hybrid finite volume-finite element discretization scheme, this test function corresponds to ϕ_i for finite elements and ψ_i for finite volumes. Hence the equation 2.24 can be integrated as follows:

$$\int_{\Pi_i} \frac{\partial(\rho C_a)}{\partial t} d\sigma + \int_{\Pi_i} \vec{\nabla} \cdot (\rho C_a \vec{V}) d\sigma = 0, \qquad \forall \ \Pi_i \in \Omega \qquad 2.24$$

Integration of the equation 2.25 for all nodes i in the domain of calculation, yields a linear system of equations which needs to be solved. In order to facilitate this integration, each term in the equation 2.25 is treated separately.

Convective term:

$$\begin{aligned}\int_{\Pi_i} \vec{\nabla}\cdot(\rho C_a \vec{V})d\sigma &= \int_{\Pi_i} \vec{\nabla}\cdot\vec{F}\,d\sigma \\ &= \int_{\partial\Pi_i} \vec{F}\cdot\vec{n}\,d\sigma \\ &= \sum_{t=1}^{T} \vec{F}_{i,t}\cdot\vec{n}_{i,t}\partial s_{i,t}\end{aligned} \qquad 2.25$$

with,

$$\partial\Pi_i = \bigcup_{t=1}^{T} \partial s_{i,t}$$

T - Total number of nodes surrounding vertex i

Temporal term:

$$\int_{\Pi_i} \frac{\partial(\rho C_a)}{\partial t} d\sigma = \frac{\partial(\rho_i C_{a_i})}{\partial t}\sigma_{\Pi_i} \qquad 2.26$$

Temporal discretization:

The first-order Euler Backward implicit scheme is used for the numerical time marching which this yields a nonlinear system of equations. However, in order to avoid using a nonlinear solver, the equations are linearized using the first order Taylor expansion. Equation 2.25 now can be discretized as follow:

$$\begin{aligned}\frac{\partial(\rho_i C_{a_i})}{\partial t} &= \frac{(\rho_i C_{a_i})^{n+1} - (\rho_i C_{a_i})^n}{\Delta t} - \frac{\rho_i^{n+1} C_{a_i}^n}{\Delta t} + \frac{\rho_i^{n+1} C_{a_i}^n}{\Delta t} \\ &= \frac{\rho_i^{n+1}\Delta C_{a_i}^{n+1}}{\Delta t} - \frac{\rho_i^n C_{a_i}^n}{\Delta t} + \frac{\rho_i^{n+1} C_{a_i}^n}{\Delta t}\end{aligned}$$

then,

$$(\frac{\rho_i^{n+1}\Delta C_{a_i}^{n+1}}{\Delta t}-\frac{\rho_i^{n}C_{a_i}^{n}}{\Delta t}+\frac{\rho_i^{n+1}C_{a_i}^{n}}{\Delta t})\sigma_{\Pi_i}+\sum_{t=1}^{T}\vec{F}_{i,t}^{n+1}\cdot\vec{n}_{i,t}\partial s_{i,t}=0$$

Using the aforementioned Taylor's expansion, the convective flux vector is linearized

$$\vec{F}^{n+1}=\vec{F}^{n}+\frac{\partial\vec{F}^{n}}{\partial C_a}\Delta C_a^{n+1}=\vec{F}^{n}+\vec{A}^{n}\Delta C_a^{n+1}$$

with $\vec{A}^{n}$ being,

$$\vec{A}^{n}=\rho^{n}\vec{V}^{n}$$

and,

$$\sum_t\vec{F}^{n+1}\cdot\vec{n}\partial s=\sum_t\vec{F}^{n}\cdot\vec{n}\partial s+\sum_t\vec{A}^{n}\Delta C_a^{n+1}\cdot\vec{n}\partial s$$

Hence,

$$(\frac{\rho_i^{n+1}\Delta C_{a_i}^{n+1}}{\Delta t}-\frac{\rho_i^{n}C_{a_i}^{n}}{\Delta t}+\frac{\rho_i^{n+1}C_{a_i}^{n}}{\Delta t})\sigma_{\Pi_i}+\sum_{t=1}^{T}\vec{F}_{i,t}^{n}\cdot\vec{n}_{i,t}\partial s_{i,t}+\sum_{t=1}^{T}\vec{A}^{n}\Delta C_{a_i}^{n+1}\cdot\vec{n}_{i,t}\partial s_{i,t}=0$$

And finally,

$$(\frac{\rho_i^{n+1}}{\Delta t}\sigma_{\Pi_i}+\sum_{t=1}^{T}\vec{A}_{i,t}^{n}\cdot\vec{n}_{i,t}\partial s_{i,t})\Delta C_{a_i}^{n+1}=(\frac{\rho_i^{n}C_{a_i}^{n}}{\Delta t}-\frac{\rho_i^{n+1}C_{a_i}^{n}}{\Delta t})\sigma_{\Pi_i}-\sum_{t=1}^{T}\vec{F}_{i,t}^{n}\cdot\vec{n}_{i,t}\partial s_{i,t}\qquad 2.27$$

Convective flux calculations:

To be consistent with the Euler Solver code being extended, the Roe's approximate Riemann Solver scheme is used for the purpose of flux calculations. This method is based on characteristics decomposition of the flux differences across discontinuities while ensuring the conservation properties of the scheme, [38]. Having introduced the convective flux vector in equation 2.27, the numerical flux between two neighbor cell vertices can be determined based on Roe's scheme as follows:

$$\vec{F} = \rho C_a \vec{V} \qquad 2.28$$

$$\vec{F}_{i,j} = \tfrac{1}{2}\left[(\vec{F}^{+}\cdot\vec{n}_{i,j}) + (\vec{F}^{-}\cdot\vec{n}_{i,j})\right] + \tfrac{1}{2}\left|\rho\vec{V}\cdot\vec{n}_{i,j}\right|(C_a^{+} - C_a^{-}) \qquad 2.29$$

Using the nodal values in the above equation yields a first order spatial scheme for convective term. However, by means of a linear interpolation of the flow variables at the middle of the edge connecting two neighbor cell vertices a second order spatial approximation can be achieved for the convective term.

$$C_a^{+} = C_{a_j} - \tfrac{1}{2}\vec{\nabla}C_{a_j}\cdot\vec{x}_{i,j} \quad , \quad C_a^{-} = C_{a_i} + \tfrac{1}{2}\vec{\nabla}C_{a_i}\cdot\vec{x}_{i,j}$$

$$\vec{V}^{+} = \vec{V}_j - \tfrac{1}{2}\vec{\nabla}\vec{V}_j\cdot\vec{x}_{i,j} \quad , \quad \vec{V}^{-} = \vec{V}_i + \tfrac{1}{2}\vec{\nabla}\vec{V}_i\cdot\vec{x}_{i,j}$$

$$\vec{F}^{+} = \rho^{+}C_a^{+}\vec{V}^{+} \quad , \quad \vec{F}^{-} = \rho^{-}C_a^{-}\vec{V}^{-}$$

$$\vec{x}_{i,j} = \vec{x}_j - \vec{x}_i$$

The gradients of flow variables introduced in the above relationships can be computed using the following method which is based on a finite element technique, [37].

$$\vec{\nabla}C_{a_j} = \frac{\int_{\Pi_j} \vec{\nabla}(C_a\varphi)d\sigma}{\int_{\Pi_j} d\sigma} = \frac{1}{\sigma_{\Pi_j}} \int_{\Omega_j} \vec{\nabla}(C_a\varphi)d\sigma$$

$$\int_{\Omega_j} \vec{\nabla}(C_a\varphi)d\sigma = \sum_{r=1}^{R_j} \int_{\omega_r} \vec{\nabla}(C_a\varphi)d\sigma = \sum_{e=1}^{E} \int_{\omega_e} \vec{\nabla}(C_a\varphi)d\sigma$$

$$\int_{\omega_e} \vec{\nabla}(C_a\varphi)d\sigma = \tfrac{1}{4} \int_{\omega_e} \vec{\nabla}(\sum_{k=1}^{4} C^e_{a_k}\varphi^e_k)d\sigma = \tfrac{1}{4}\sum_{k=1}^{4} \int_{\omega_e} \vec{\nabla}(C^e_{a_k}\varphi^e_k)d\sigma$$

$$= \tfrac{1}{4}\sum_{k=1}^{4} \int_{\omega_e} C^e_{a_k}\vec{\nabla}\varphi^e_k\, d\sigma$$

$$= \tfrac{1}{4}\sum_{k=1}^{4} C^e_{a_k}\vec{\nabla}\varphi^e_k\sigma_{\omega_e}$$

where,

$\sigma \equiv$ Volume of the finite element ω_e

Finally the gradients can be written as follows:

$$\vec{\nabla}C_{a_j} = \frac{1}{\sigma_{\Pi_j}}\sum_{e=1}^{E}\frac{\sigma_{\omega_e}}{4}\sum_{k=1}^{4} C^e_{a_k}\vec{\nabla}\varphi^e_k$$

$$\vec{\nabla}C_{a_i} = \frac{1}{\sigma_{\Pi_i}}\sum_{e=1}^{E}\frac{\sigma_{\omega_e}}{4}\sum_{k=1}^{4} C^e_{a_k}\vec{\nabla}\varphi^e_k$$

$$\vec{\nabla}u_i = \frac{1}{\sigma_{\Pi_i}}\sum_{e=1}^{E}\frac{\sigma_{\omega_e}}{4}\sum_{k=1}^{4} u^e_{a_k}\vec{\nabla}\varphi^e_k$$

$$\vec{\nabla}v_i = \frac{1}{\sigma_{\Pi_i}}\sum_{e=1}^{E}\frac{\sigma_{\omega_e}}{4}\sum_{k=1}^{4} v^e_{a_k}\vec{\nabla}\varphi^e_k$$

$$\vec{\nabla}w_i = \frac{1}{\sigma_{\Pi_i}}\sum_{e=1}^{E}\frac{\sigma_{\omega_e}}{4}\sum_{k=1}^{4} w^e_{a_k}\vec{\nabla}\varphi^e_k$$

2.3.2 Discretization of the source term in the Euler equations

For the spatial discretization of the source term in the Euler equations finite element technique is applied. Considering the following source vector S due to gravity acceleration in momentum and energy equations, it can be integrated in the same manner as the diffusion term in the species transport equation.

$$S = \begin{pmatrix} 0 \\ \rho g_x \\ \rho g_y \\ \rho g_z \\ \rho \vec{V} \cdot \vec{g} \end{pmatrix} \qquad 2.30$$

Momentum source term:

$$\int_{\Omega_i} \rho \vec{g} \varphi_i d\sigma = \sum_{r=1}^{R_i} \int_{\omega_r} \rho \vec{g} \varphi_i d\sigma = \sum_{e=1}^{E} \int_{\omega_e} \rho \vec{g} \varphi_i d\sigma \qquad 2.31$$

Defining the following field variable,

$$\rho = \sum_{i=1}^{N} \rho_i \lambda_i ,$$

integrating equation

$$\int_{\Omega_i} \rho\vec{g}\varphi_i d\sigma = \sum_{r=1}^{R_i} \int_{\omega_r} \rho\vec{g}\varphi_i d\sigma = \sum_{e=1}^{E} \int_{\omega_e} \rho\vec{g}\varphi_i d\sigma \qquad 2.31$$

$$\int_{\omega_e} \rho\vec{g}\varphi_i d\sigma = \vec{g}\int_{\omega_e} \varphi_i \sum_t \rho_t\lambda_t d\sigma = \vec{g}\sum_t \rho_t \int_{\omega_e} \varphi_i\lambda_t d\sigma$$

and finally,

$$\int_{\Omega_i} \rho\vec{g}\varphi_i d\sigma = \vec{g}\sum_{e=1}^{E}\sum_t \rho_t M_{i,t}^e \qquad 2.32$$

where,

$$M_{i,t}^e = \int_{\omega_e} \varphi_i\lambda_t d\sigma$$

Energy source term:

$$\int_{\Omega_i} \rho\vec{V}\cdot\vec{g}\varphi_i d\sigma = \int_{\Omega_i} \rho(ug_x + vg_y + wg_z)\varphi_i d\sigma \qquad 2.33$$

For the x-axis component the above integral can be numerically computed as follows:

$$\int_{\Omega_i} \rho u g_x \varphi_i d\sigma = \sum_{r=1}^{R_i} \int_{\omega_r} \rho u g_x \varphi_i d\sigma = \sum_{e=1}^{E} \int_{\omega_e} \rho u g_x \varphi_i d\sigma$$

$$\int_{\omega_e} \rho u g_x \varphi_i d\sigma = g_x \int_{\omega_e} \rho u \varphi_i d\sigma$$

defining the field variable,

$$\rho u = Y = \sum_{i=1}^{N} Y_i \phi_i$$

then,

$$\begin{aligned}\int_{\omega_e} \rho u g_x \varphi_i d\sigma &= g_x \int_{\omega_e} Y \varphi_i d\sigma \\ &= g_x \int_{\omega_e} \left(\sum_r Y_r \lambda_r \right) \varphi_i d\sigma \\ &= g_x \sum_r Y_r \int_{\omega_e} \lambda_r \varphi_i d\sigma\end{aligned}$$

finally,

$$\int_{\Omega_i} \rho u g_x \varphi_i d\sigma = g_x \sum_{e=1}^{E} \sum_{r=1}^{N} \rho_r u_r M_{r,i}^e \qquad 2.34$$

In the same manner for the y-axis and z-axis direction this integration can be completed.

$$\int_{\Omega_i} \rho v g_y \varphi_i d\sigma = g_y \sum_{e=1}^{E} \sum_{r=1}^{N} \rho_r v_r M_{r,i}^e \qquad 2.35$$

$$\int_{\Omega_i} \rho w g_z \varphi_i d\sigma = g_z \sum_{e=1}^{E} \sum_{r=1}^{N} \rho_r w_r M_{r,i}^e \qquad 2.36$$

Source term-contribution to the Jacobian matrix:

Using the previously mentioned first order backward time integration, the source vector is written as below:

$$S(U)^{n+1} = S(U)^n + \left(\frac{\partial S}{\partial U}\right)^n \cdot \Delta U^{n+1}$$

In order to compute the contribution of the source terms to the Jacobian matrix, first the flux vector obtained in equations 2.36, and 2.38 to 2.40 are rewritten in terms of conservative variables. Defining the conservative variables:

$$U = \begin{pmatrix} \rho \\ \rho u \\ \rho v \\ \rho w \\ \rho E \end{pmatrix} = \begin{pmatrix} \rho \\ m \\ n \\ l \\ \varepsilon \end{pmatrix} \qquad 2.37$$

and considering the source flux vector,

$$S = \begin{pmatrix} 0 \\ g_x \sum_{e=1}^{E} \sum_{t} \rho_t M_{i,t}^e \\ g_y \sum_{e=1}^{E} \sum_{t} \rho_t M_{i,t}^e \\ g_z \sum_{e=1}^{E} \sum_{t} \rho_t M_{i,t}^e \\ g_x \sum_{e=1}^{E} \sum_{r=1}^{N} \rho_r u_r M_{r,i}^e + g_y \sum_{e=1}^{E} \sum_{r=1}^{N} \rho_r v_r M_{r,i}^e + g_z \sum_{e=1}^{E} \sum_{r=1}^{N} \rho_r w_r M_{r,i}^e \end{pmatrix} \qquad 2.38$$

in terms of conservative variables it can be rewritten as,

$$S=\begin{pmatrix} 0 \\ g_x \sum_{e=1}^{E}\sum_{t}\rho_t M_{i,t}^{e} \\ g_y \sum_{e=1}^{E}\sum_{t}\rho_t M_{i,t}^{e} \\ g_z \sum_{e=1}^{E}\sum_{t}\rho_t M_{i,t}^{e} \\ g_x \sum_{e=1}^{E}\sum_{r=1}^{N} m_r M_{r,i}^{e} + g_y \sum_{e=1}^{E}\sum_{r=1}^{N} n_r M_{r,i}^{e} + g_z \sum_{e=1}^{E}\sum_{r=1}^{N} l_r M_{r,i}^{e} \end{pmatrix}$$

The Jacobian matrix then will be:

$$\frac{\partial S}{\partial U}=\begin{bmatrix} \frac{\partial S_1}{\partial \rho} & \frac{\partial S_1}{\partial m} & \frac{\partial S_1}{\partial n} & \frac{\partial S_1}{\partial l} & \frac{\partial S_1}{\partial \varepsilon} \\ \frac{\partial S_2}{\partial \rho} & \frac{\partial S_2}{\partial m} & \frac{\partial S_2}{\partial n} & \frac{\partial S_2}{\partial l} & \frac{\partial S_2}{\partial \varepsilon} \\ \frac{\partial S_3}{\partial \rho} & \frac{\partial S_3}{\partial m} & \frac{\partial S_3}{\partial n} & \frac{\partial S_3}{\partial l} & \frac{\partial S_3}{\partial \varepsilon} \\ \frac{\partial S_4}{\partial \rho} & \frac{\partial S_4}{\partial m} & \frac{\partial S_4}{\partial n} & \frac{\partial S_4}{\partial l} & \frac{\partial S_4}{\partial \varepsilon} \\ \frac{\partial S_5}{\partial \rho} & \frac{\partial S_5}{\partial m} & \frac{\partial S_5}{\partial n} & \frac{\partial S_5}{\partial l} & \frac{\partial S_5}{\partial \varepsilon} \end{bmatrix} \qquad 2.39$$

$$=\left(\sum_{e=1}^{E} M_{i,t}^{e}\right)\begin{bmatrix} 0 & 0 & 0 & 0 & 0 \\ g_x & 0 & 0 & 0 & 0 \\ g_y & 0 & 0 & 0 & 0 \\ g_z & 0 & 0 & 0 & 0 \\ 0 & g_x & g_y & g_z & 0 \end{bmatrix}$$

2.4 Boundary conditions

There are two types of boundaries used in this study, slip solid wall, and the non-reflecting far field boundary. For the walls of hydrogen vessel and also for the rear wall (the wall with the orifice) the slip solid surfaces are used. The remaining boundaries of the computational domain are set as non-reflecting far field. More discussion on boundary conditions is reported in section 3.3 of the next chapter.

3

Validation and Analysis of the Results

In this chapter,

the numerical results obtained based on the methods described in the previous chapter are compared to available data corresponding to the same physical initial and boundary conditions. After this validation, results for release from 800-bar vessel are studied.

3.1 Validation method

Our aim is to simulate the hydrogen release from an 800-bar pressure vessel. However, before proceeding with this simulation we need to verify that the code is able to solve such a highly underexpanded jet flow. This is done by comparison of the results of the code and the similar available data. As mentioned in chapter 1, due to technical difficulties associated with measurement of very rapid changes of flow pattern and properties in the region close to the exit nozzle the experimental investigation of underexpanded jets are restricted to schlieren photography methods and global quantities such as Mach disk location. Even the advent of new technologies such as laser anemometry has not made it possible to accurately measure the flow variables in the near-field region. Hence, most of the numerical simulations of underexpanded jets are compared with the results from characteristic methods and global quantities from imagery experiments. In this thesis we compare the results obtained from our CFD code with the corresponding data from the numerical study by Pedro et al, [25], using Fluent commercial code, in which a hydrogen jet is modeled after release from a high pressure vessel into a hydrogen medium.

In that simulation the hydrogen initial pressure inside the vessel is at 100 bars and 300-K temperature. It is assumed that the gas exits a 5-mm diameter orifice into hydrogen medium at the same temperature but atmospheric pressure of 101325 Pa. To compare our own results with this simulation we consider the same initial conditions. In

addition the gravity acceleration effects are also ignored. This postulation is quite reasonable since at the very early period of high pressure gas release the momentum exerted on the fluid due to gravity is essentially negligible in comparison with the momentum produced by high pressure upstream source. This assumption is also applied in [25].

3.2 Computational domain geometry and meshing

The complete 3D physical geometry is composed of a circular cylinder of 0.264 L volume with the radius of 0.1m and height of 0.2m as the medium chamber which is connected to a high pressure vessel via a 5-mm diameter opening. Taking advantage of axisymmetry property of the free round jet a 60-degree slice of the physical domain, as shown in Figure 3.1, is considered for the computational domain.

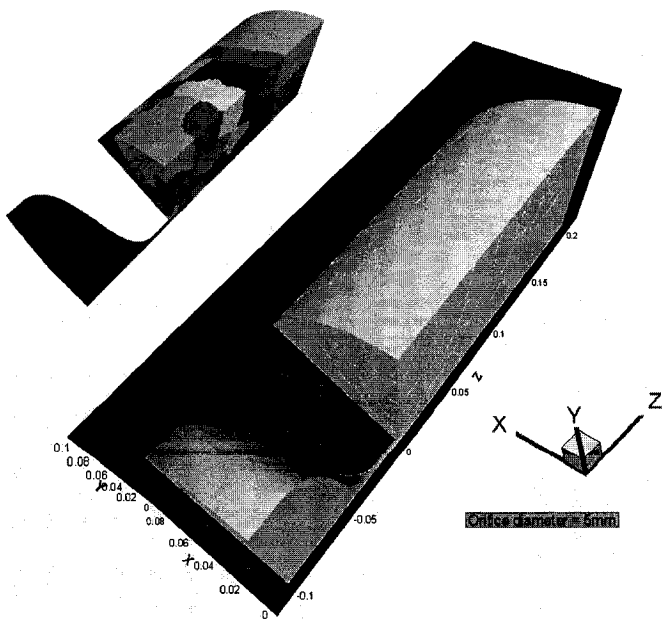

Figure 3.1 60-degree slice computational domain and the decomposed mesh

This helps us to use a finer mesh for a better shock capturing. The computational domain is then meshed using Gambit mesh generator software by 4-node unstructured tetrahedral elements with the purpose of being compatible with the extended Euler solver discussed earlier. In order to accurately capture rapid changes in the flow field variables in the region close to the release point, where critical flow conditions exist, very fine mesh grids are required at that region. In order to illustrate mesh grids that is used, a slice view of the mesh is shown in Figure 3.2-a to c.

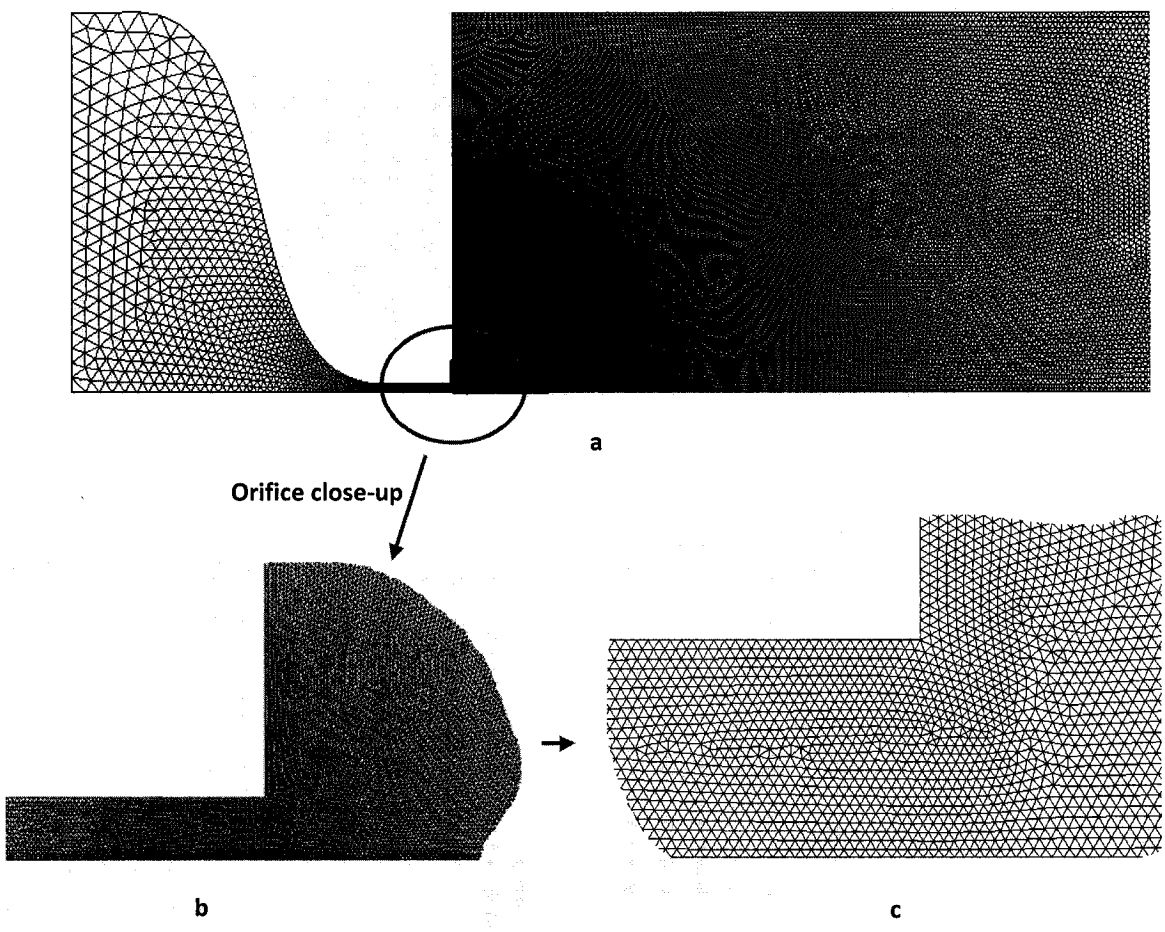

Figure 3.2 A slice view of the mesh which is used.

The critical flow conditions at the release point along with the small size of the orifice makes this domain extremely difficult to mesh. The difficulty is due to the fact that Gambit only provides linear size functions which makes it hard to have very fine mesh grids near the orifice and coarser grid resolution in other regions where flow exhibits less critical behavior. The finest mesh that is possible to construct with the available computational resources has 4 million nodes generated on Cirrus (Concordia University's Supercomputer) by using 64GB of memory. The mesh generated is then decomposed into 64 sub-domains, as also shown in Figure 3.1, to be run in parallel on Cirrus. The Euler solver is already parallelized by using Message Passing Interface (MPI) method. To be consistent with the core solver, the subroutines which are added to the code for solution of species conservation equation are made parallel with the same standards.

3.3 Boundary conditions

As previously mentioned in chapter 2, two types of boundary conditions are applied in this simulation. The slipping solid wall boundary is used for the walls inside the vessel as well as for the rear wall which has the orifice. This slipping boundary condition is consistent with inviscid flow assumption. For all other physical boundaries the non-reflecting boundary type is implemented to prevent any non-physical wave reflection. Furthermore, since the computational domain a cut of the physical domain, a condition has to be applied to the side surfaces of computational slice. In the absence of any

source of disturbances which could alter the symmetry property of the flow of our interest around the jet axis, no streamline of the flow can pass across the side surfaces of the 60-degree computational slice. Therefore we can completely model these artificial boundaries by the same slipping boundaries used for solid walls.

3.4 Some computational issues

During the course of this research project some issues came up which we did not find any satisfactory approaches so that we had to address alternatives. We list them below as guidelines for future works discussed in chapter 4.

3.4.1 Supersonic inlet

Mohamed et al., [26], simulated the flow at the exit of a hole through a high pressure vessel. They have prepared a computer code which is able to calculate the flow conditions at the nozzle exit based on the physical geometry and initial conditions as a function of time. We had intended to append their code to our Euler solver with the aim of saving computational time and resources. However, due to lack of supersonic inlet boundary type in our code we preferred to simulate the whole domain including the pressure vessel together to avoid the need for implementation of supersonic inlet. Fortunately because of the relatively simple flow inside the pressure tank even a coarse mesh is quite satisfactory for the flow inside the vessel so it was not as expensive as previously thought.

3.4.2 Order of spatial approximation

The flux calculation method which is described in section 2.3.1 and used in the Euler solver is capable of both first and second-order approximations. Nevertheless, when we apply the second-order interpolation for high pressure gas release problem the solution becomes unstable and eventually the code crashed. The result is the same even when the van Albada flux limiter (which is already exists in the code) is applied to damp off the numerical oscillations. The author also tried a few other combinations of methods of calculation gradients and flux limiters as suggested by Jawahar, [39], TU, [40], Cueto-Felgueroso, [41], but could not obtain a scheme for second-order approximations which is able to preserve the second-order level of accuracy at smooth region and damp the non-physical oscillations at discontinuities. Hence, we chose to use first-order accurate fluxes.

3.4.3 Small time steps

Because of the very fine mesh grids and the very high speed flow the characteristic information travel so fast along the mesh edges. In order to capture these rapid changes the time step increments used in the linearized Euler equations have to be adjusted according to the travel speed of characteristics. This makes the physical time steps so small (to the order of 10^{-9}-10^{-6}) such that it becomes extremely difficult to reach later times of the high pressure gas release. However, since we are interested in the early

evolution of the highly underexpanded jets which quickly become almost steady (in case of enough high stagnation pressure supply) steady, it does not make any difficulty in our near-field analysis of high-pressure gas release problem.

3.5 Verification of the results

As previously mentioned, in order to verify the validity of the results of the extended Euler solver, the obtained results are compared with corresponding data from [25]. Figure 3.3 shows the Mach number distribution along the axis of hydrogen jet in hydrogen chamber obtained from analysis done in [25]. A corresponding graph from current study is also presented in Figure 3.4. In both analyses the hydrogen gas is exiting a 100-bar reservoir at 300 K. The position of Mach disk as discussed in chapter 2 is one the key features of a highly underexpanded free jet. As it can be seen in Figure 3.3 the Mach disk is settled at $Z^*=6.5$ as obtained in [25]. This is in excellent agreement with the result of our present simulation as shown in Figure 3.4. As the exiting hydrogen flows downstream Mach disk advances along the jet axis until it get settle at an approximately steady location. The Mack disk maintains this position until the supply stagnation pressure in the vessel drops to a level at which the highly underexpanded jet converts into slightly underexpanded jet category. At this moment the Mach disk will disappear and the diamond-shaped shock cells will be formed, as previously mention in chapter 2. However, since in both present and [25] simulation the early period of the release

process is modeled we have not reached the slightly underexpanded level as shown in Figure 3.3 and Figure 3.4.

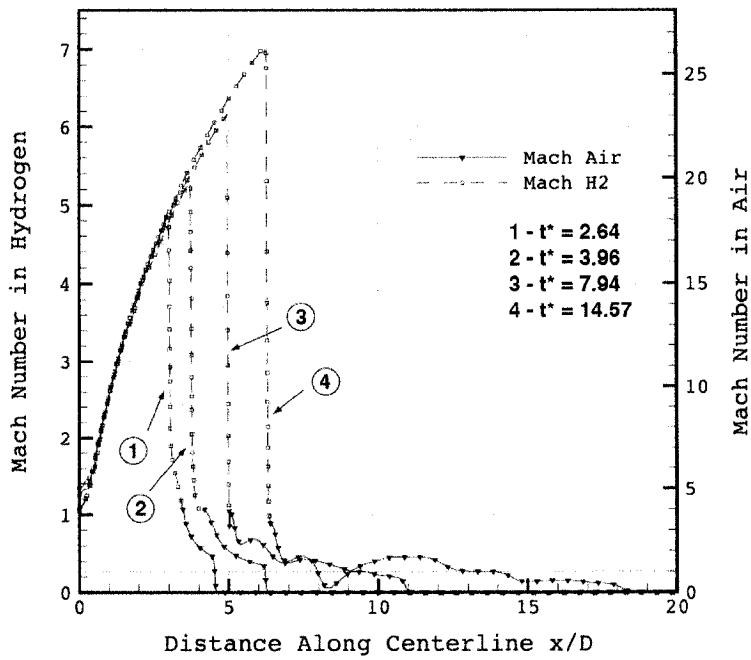

Figure 3.3 Mach number distribution along the H_2-H_2 jet at several points in times, [25].

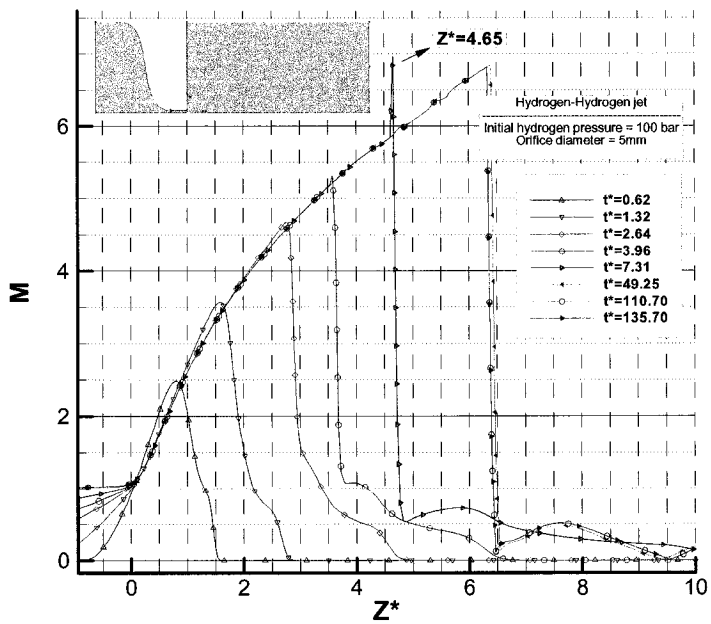

Figure 3.4 Mach number distribution along the axis of H_2-H_2 jet at different moments of release, obtained in present simulation.

The maximum Mach number which can be read from Mach distribution graph in Figure 3.3 is around 7. Although this is also confirmed in the present simulation, however, as it is seen in Figure 3.4 there is an overshoot in the Mach number distribution which is not seen in Figure 3.3. It might be because of the numerical oscillations due to the numerical scheme. This overshoot also happens in other highly underexpanded jets simulated in this study and can be seen in the sections 3.6 and 3.7 in this chapter. Table 3.1 andTable 3.2 show the values for Mach disk location and the Maximum Mach number at Mach disk location read from Figure 3.3 and Figure 3.4.

t*	2.64	3.96	Quasi-steady
Fluent	3	3.8	6.2
Our code	2.89	3.63	6.4

Table 3.1 Mack disk location in H2-H2 jet

t*	2.64	3.96	Quasi-steady
Fluent	≈ 4.8	5.2	7
Our code	4.7	5.25	6.8

Table 3.2 Max. Mach number at Mack disk location

Another important point which helps us verify the validity of the extended Euler solver is the sonic flow at the exit of the release orifice. Due to chocked flow inside the pressure vessel the flow of hydrogen cannot expand and increase its speed beyond the

sound speed. Hence it can only leave the orifice at the Mach number of 1. This can easily be seen from the sets of simulation data in Figure 3.3 and Figure 3.4. An essential point which needs to be noticed about Pedro's simulation, [25], is the use of adapted mesh. This feature enables them to capture the very sharp gradients across the shock discontinuities. The sharp changes in the density ratio graphs of Figure 3.5 in comparison with the corresponding graphs in Figure 3.6 easily reveal this effect. This in fact highlights the need of implementation of a mesh adaptation technique in our solver as it will be discussed in more details in the future works of section 4.2 of chapter 4.

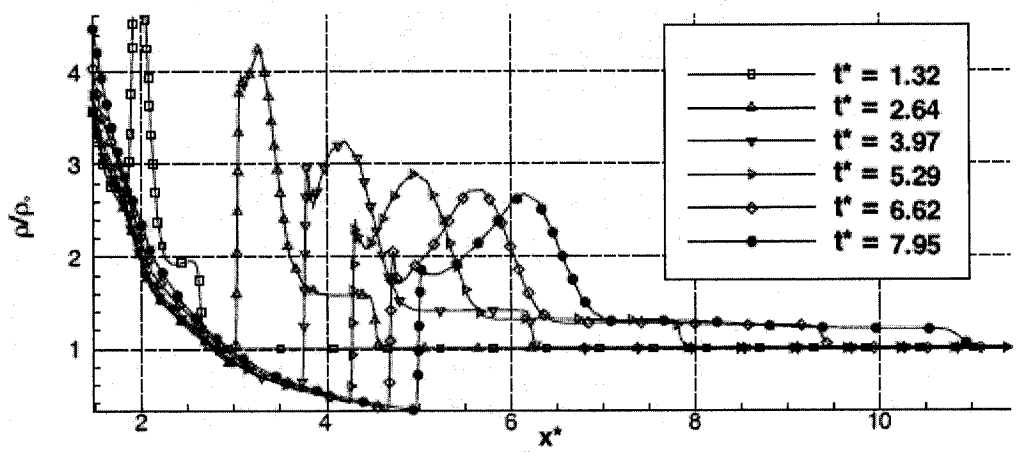

Figure 3.5 The ratio of local density along the jet centerline to the far-field density, [25].

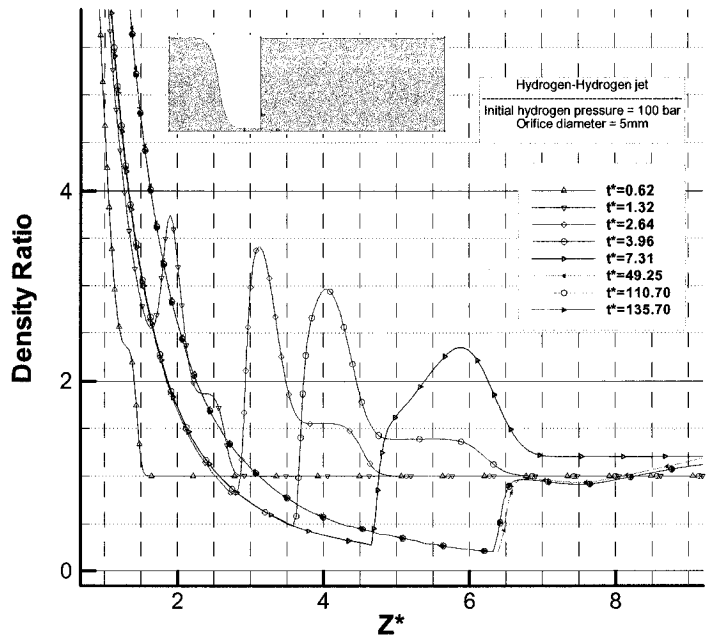

Figure 3.6 Distribution of density ratio (local to far-field) at different times during the release process.

Note that the Pedro's simulation is performed with Fluent which is based on a primitive variable formulation. This type of formulation dose not guarantee the correct location of the shocks. Nevertheless, we obtain the same location which indicates that Fluent's adaptive procedure was able to overcome this weakness.

3.6 Comparison of H_2-H_2 and H_2-air jets

After validation of the extended Euler solver we use the code to analyze the highly underexpanded jet flows of interest. Now with the aim of better understanding of effects of the ambient physical conditions on the gas flow from high pressure vessel, first two jets of hydrogen from 100-bar vessel into different mediums (hydrogen and air) are simulated and compared with each other. Figure 3.7 to Figure 3.20 show the Mach

number contours of hydrogen-hydrogen and hydrogen-air jets at different stages of jet evolution.

3.6.1 H_2-air slow progress

The first significant difference which appears when comparing these two jets is the slow progress of the hydrogen jet into air compared with the hydrogen release into hydrogen medium. This is quite reasonable since the higher density of air in comparison with hydrogen at atmospheric pressure damps more momentum from the oncoming hydrogen jet. Consequently, this will postpone the convergence of the H_2-air jet toward the steady state configuration as it can be inferred from Mach number distribution graphs of Figure 3.6 and Figure 3.21 for H_2- H_2 and H_2-air jets respectively. From Figure 3.6 one can see that the Mach disk in H_2- H_2 jet reaches its steady state location at the non-dimensional time of 49.25 while for H_2-air jet this happens at t*= 109.10. Another difference between these jets is the stronger lead shock which forms in front of the Mack disk in H_2-air jet as it is evident in the Mach contours of Figure 3.9 and Figure 3.10.

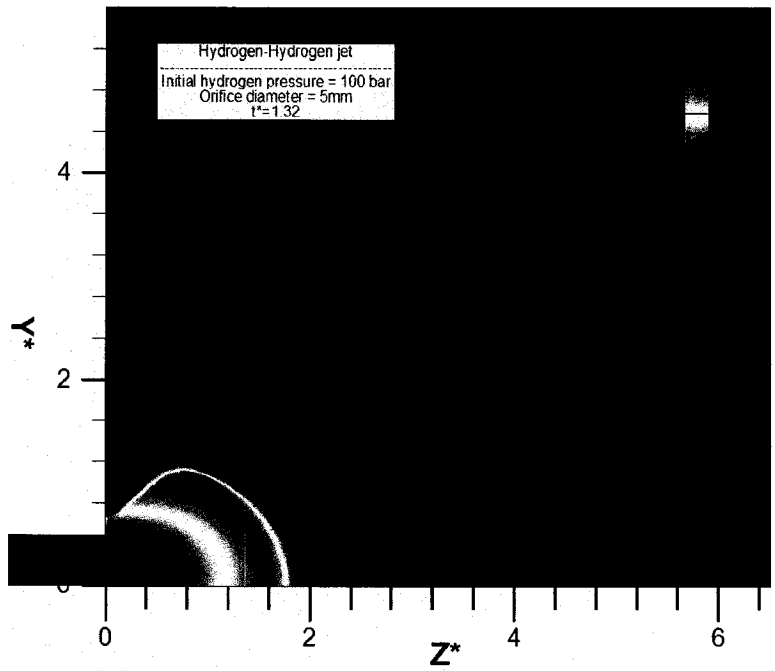

Figure 3.7 Mach number contours of hydrogen-hydrogen jet, t=1.32 (non-dim.)

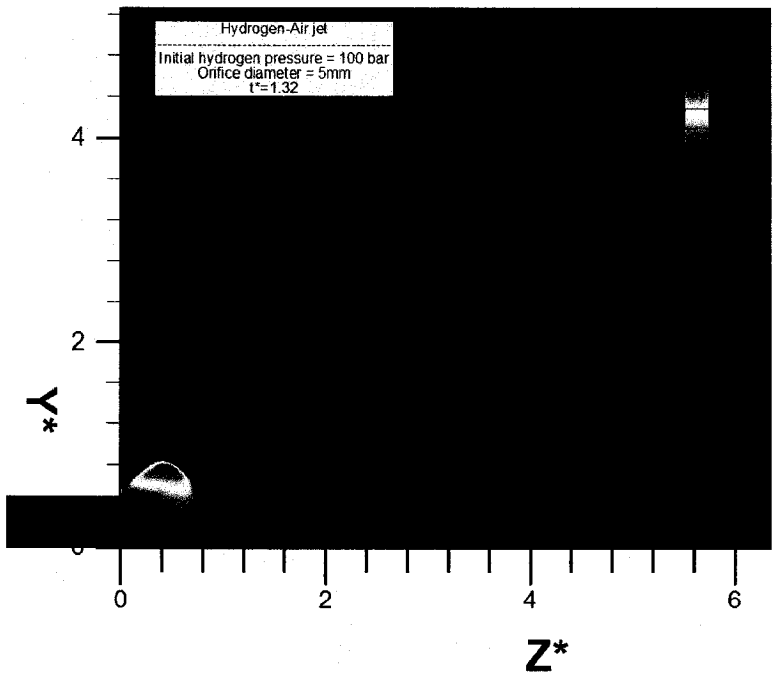

Figure 3.8 Mach number contours of hydrogen-air jet, t=1.32 (non-dim.)

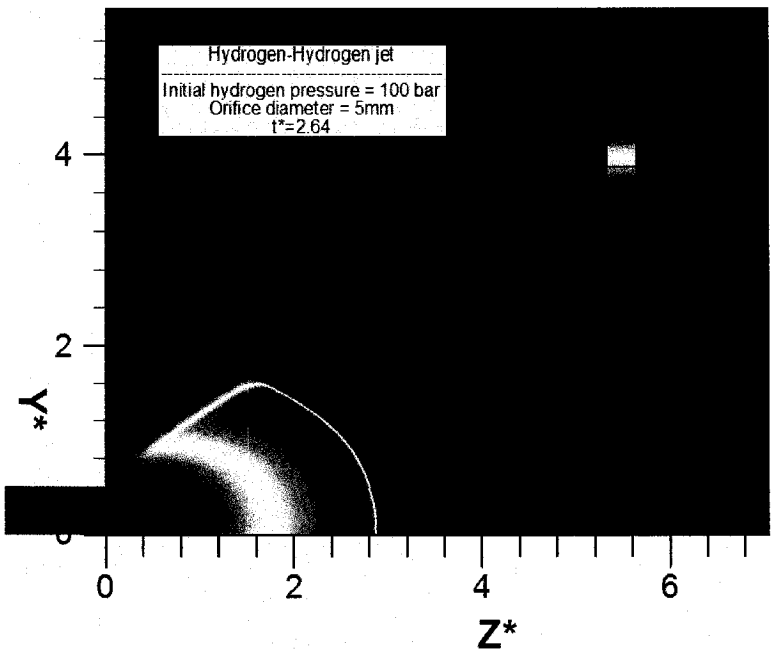

Figure 3.9 Mach number contours of hydrogen-hydrogen jet, t=2.64 (non-dim.)

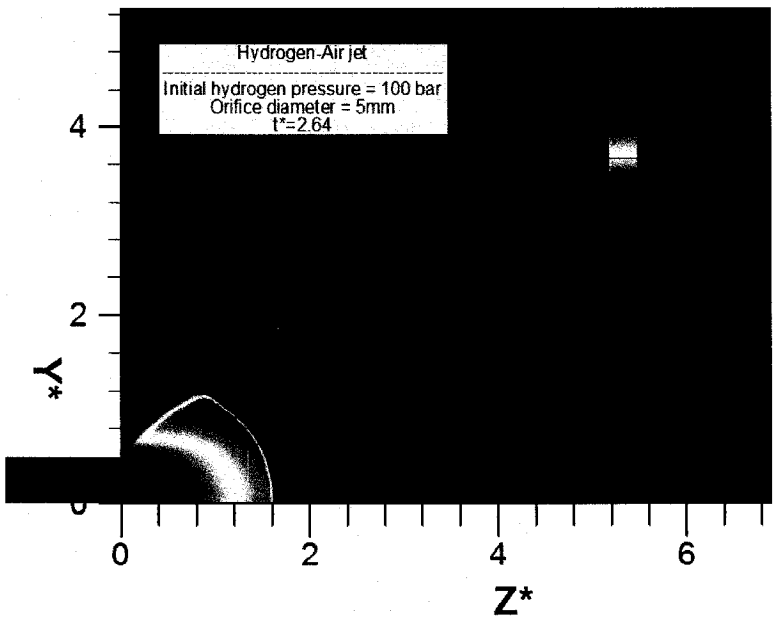

Figure 3.10 Mach number contours of hydrogen-air jet, t=2.64 (non-dim.)

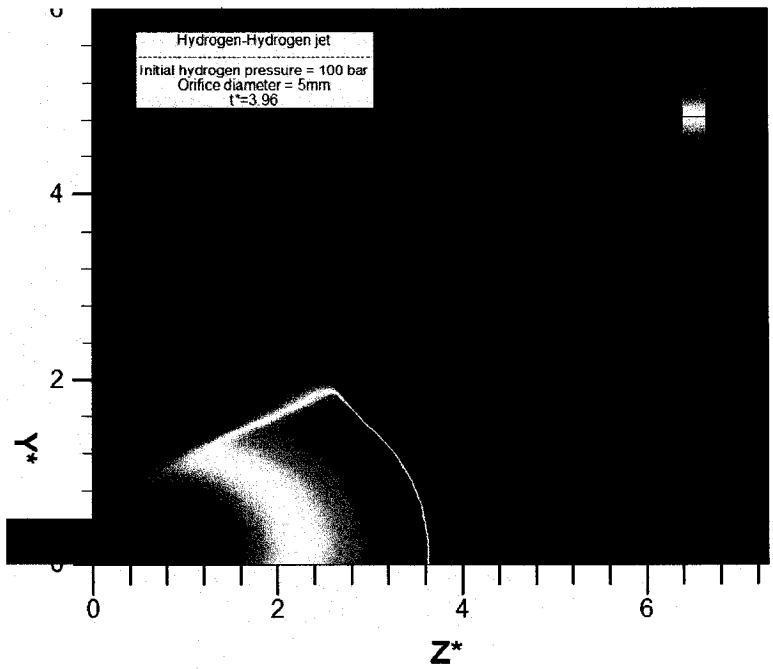

Figure 3.11 Mach number contours of hydrogen-hydrogen jet, t=3.96 (non-dim.)

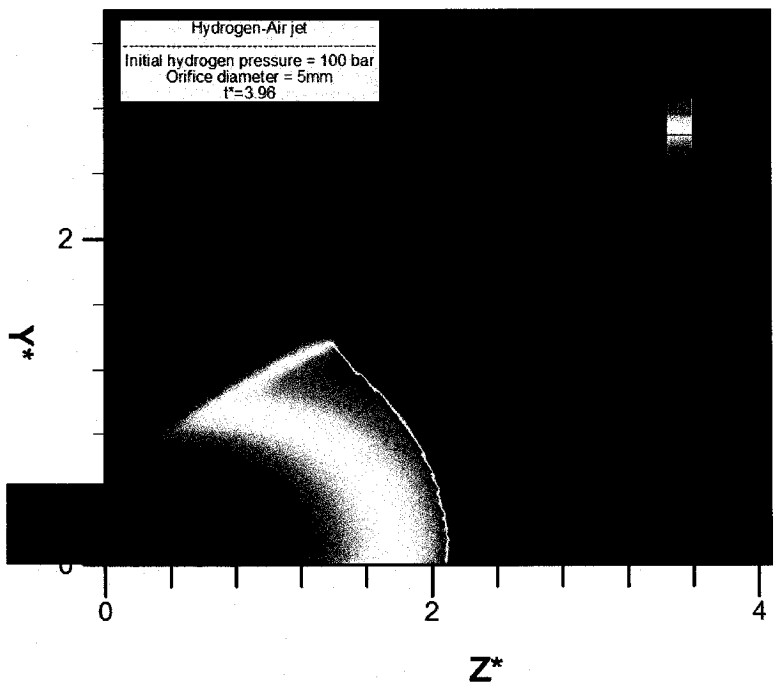

Figure 3.12 Mach number contours of hydrogen-air jet, t=3.96 (non-dim.)

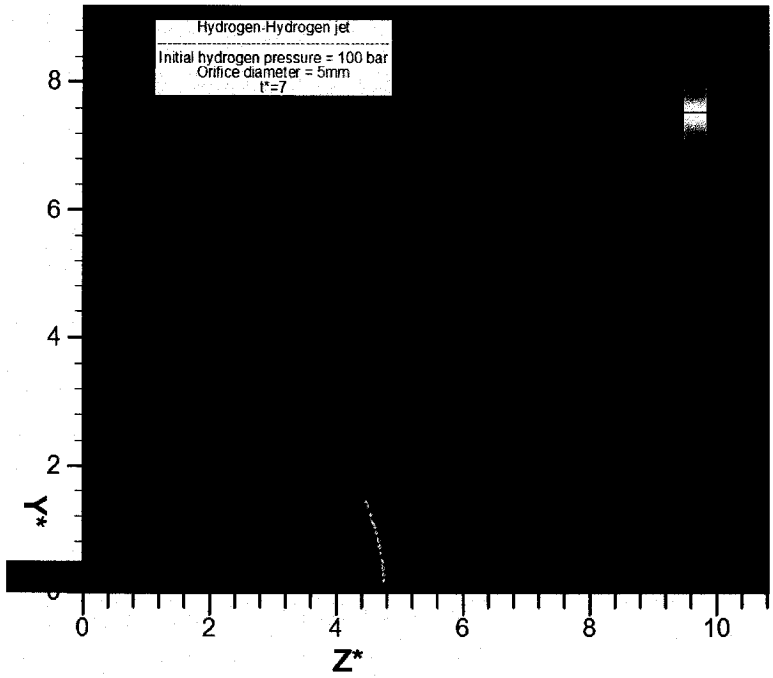

Figure 3.13 Mach number contours of hydrogen-hydrogen jet, t=7 (non-dim.)

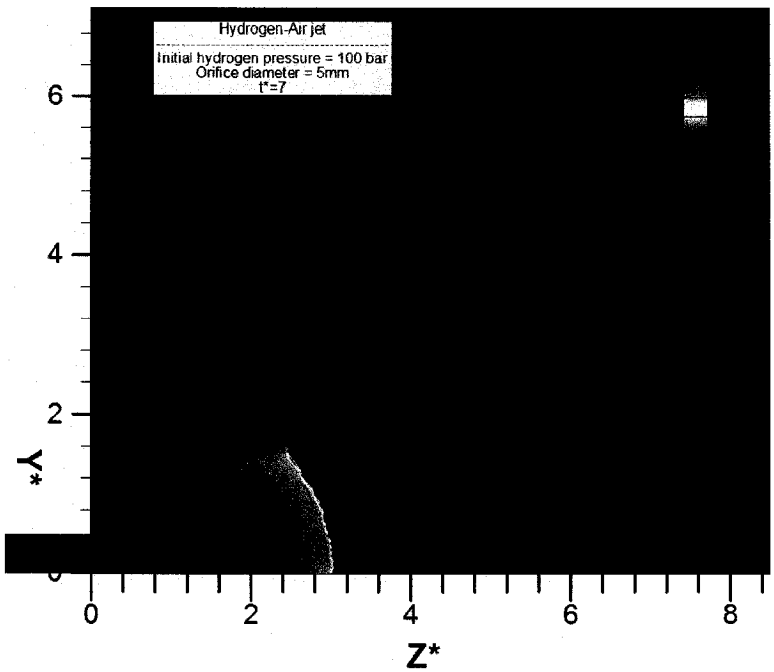

Figure 3.14 Mach number contours of hydrogen-air jet, t=7 (non-dim.)

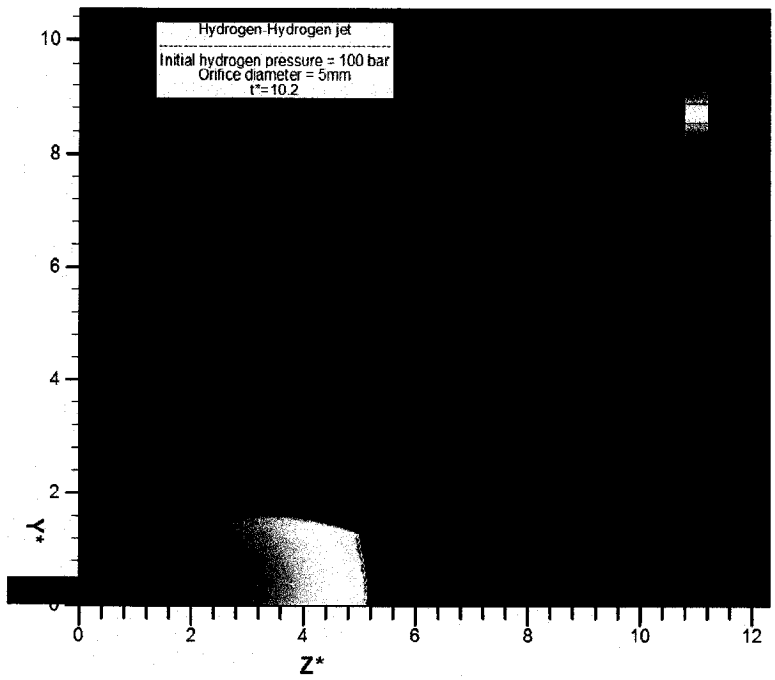

Figure 3.15 Mach number contours of hydrogen-hydrogen jet, t=10.2 (non-dim.)

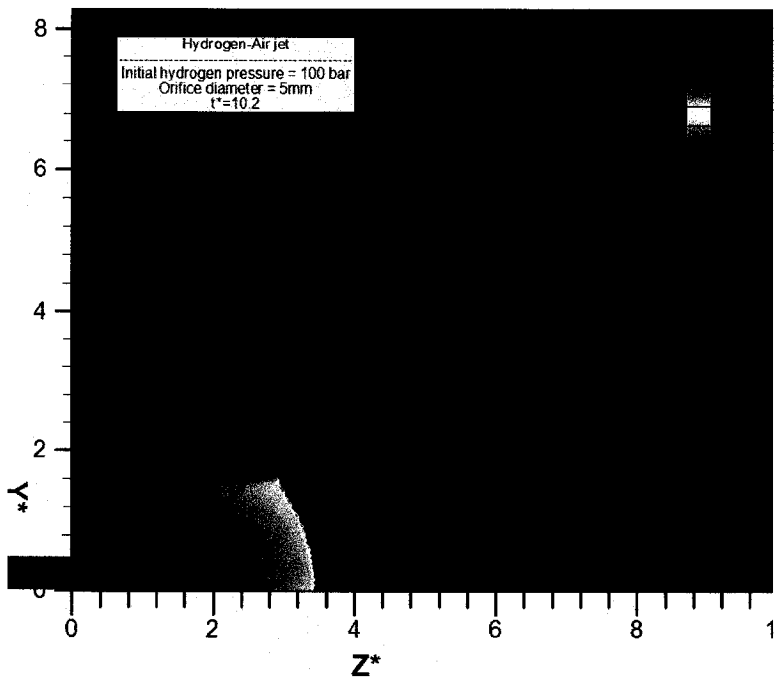

Figure 3.16 Mach number contours of hydrogen-air jet, t=10.2 (non-dim.)

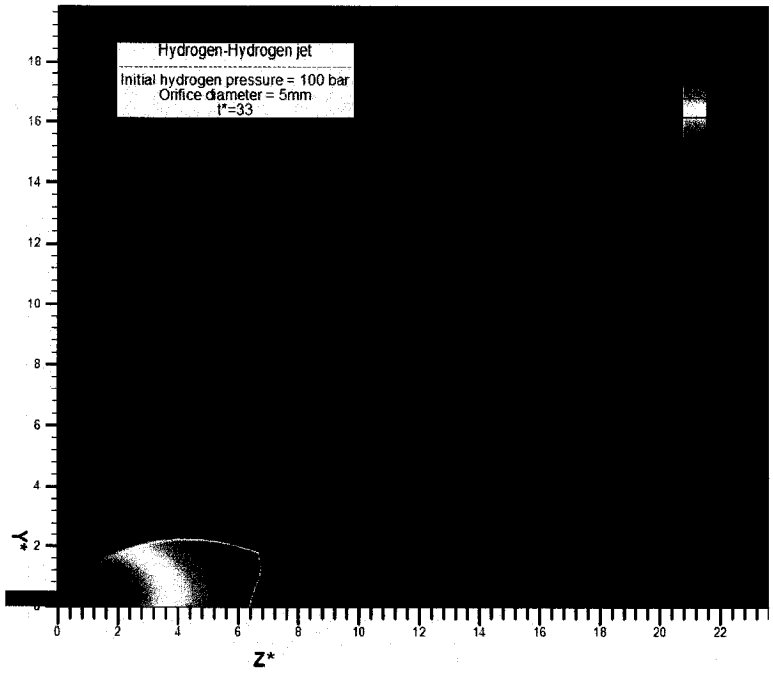

Figure 3.17 Mach number contours of hydrogen-hydrogen jet, t=33 (non-dim.)

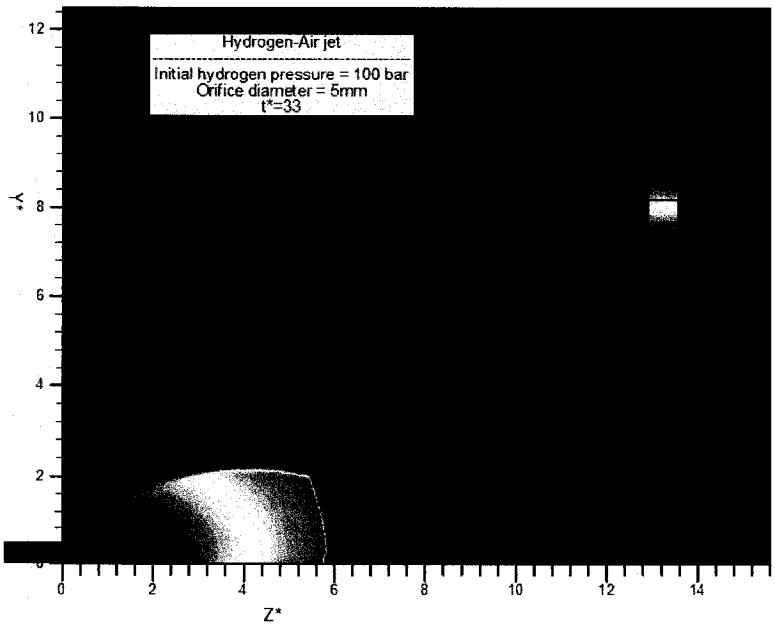

Figure 3.18 Mach number contours of hydrogen-air jet, t=33 (non-dim.)

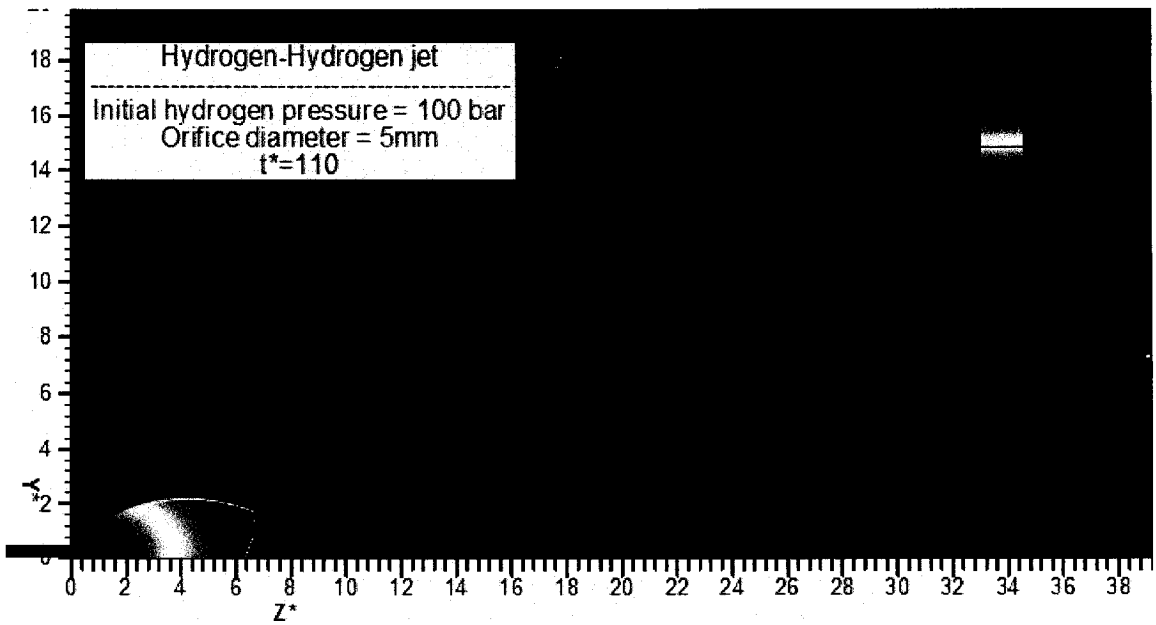

Figure 3.19 Mach number contours of hydrogen-hydrogen jet, t=110 (non-dim.)

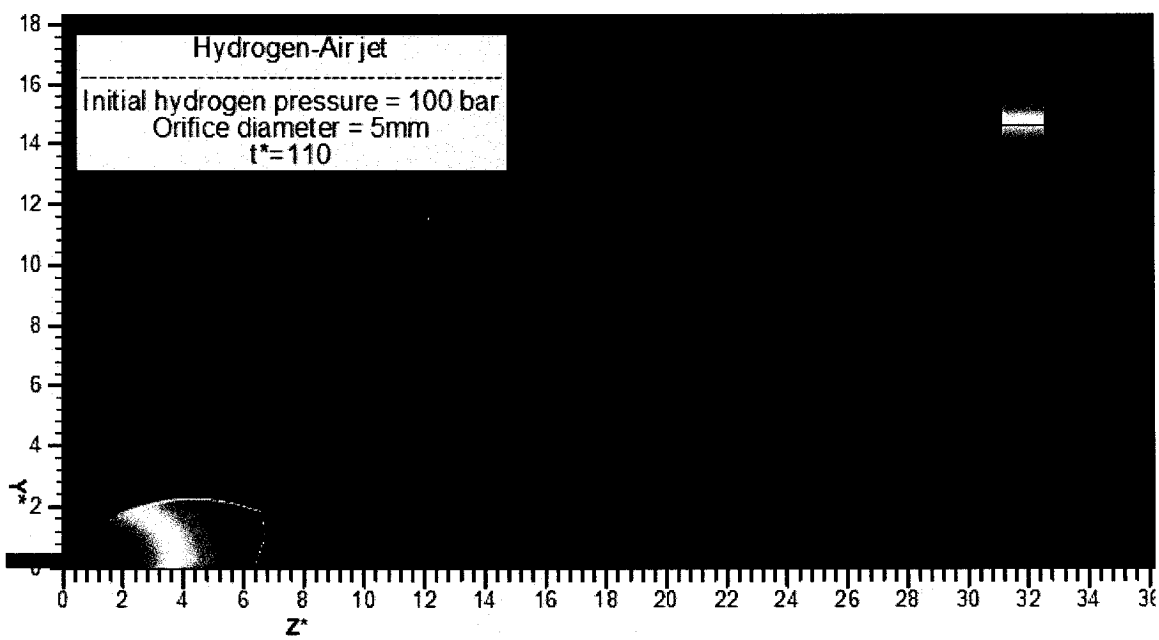

Figure 3.20 Mach number contours of hydrogen-air jet, t=110 (non-dim.)

3.6.2 Mach disk location and diameter

The comparison of settled Mach disk locations in H_2-H_2 and H_2-air jets leads to an interesting feature of the highly underexpanded free jet flow that the Mack disk location and diameter is only a function of the ratio of supply stagnation pressure to the ambient pressure. This is suggested by the following simple theoretical relationship by Young, [42].

$$\frac{Z_M}{D} = C(\gamma)\sqrt{p_0/p_a} \qquad 3.1$$

Ashkenas et al., [43], obtained $C(\gamma)$ as 0.67 through the experimental correlations. In addition, Crist et al., [44], suggested the following same formula with different coefficient for that diameter of the Mach disk.

$$\frac{Z_M}{D} = 0.24\sqrt{p_0/p_a} \qquad 3.2$$

The calculated Mach disk location and diameter from the above formulas give slightly different results (6.7 for location and 2.4 for diameter of the Mach disk) than the simulated values of the Mach disk location (6.2) and diameter (2) are the same for both hydrogen jets. Nevertheless, this can be considered as another validation of the code since both mediums give the same values.

3.6.3 Mach number distribution along the jet axis

It is also interesting to note that the Mach number distribution along the jet axis is the same for both H_2-H_2 and H_2-air jets after they become steady. This can be seen in Figure 3.4 and Figure 3.21. After non-dimension time of 49.25 in hydrogen-hydrogen jet the Mach number at Mach disk location along the jet centerline approximately becomes 6.75 and remains the same as long as there is enough pressure supply. This is also the case when the hydrogen jet is flowing into the air medium. It is good to be mentioned here that although the maximum Mach numbers in the overshoot graphs for the two jets are not the same, we cannot make any postulation about it since it might be only due to the fact that we do not record all the solutions of the code at each iteration and therefore there might be stronger overshoots happening at other moments that we have missed.

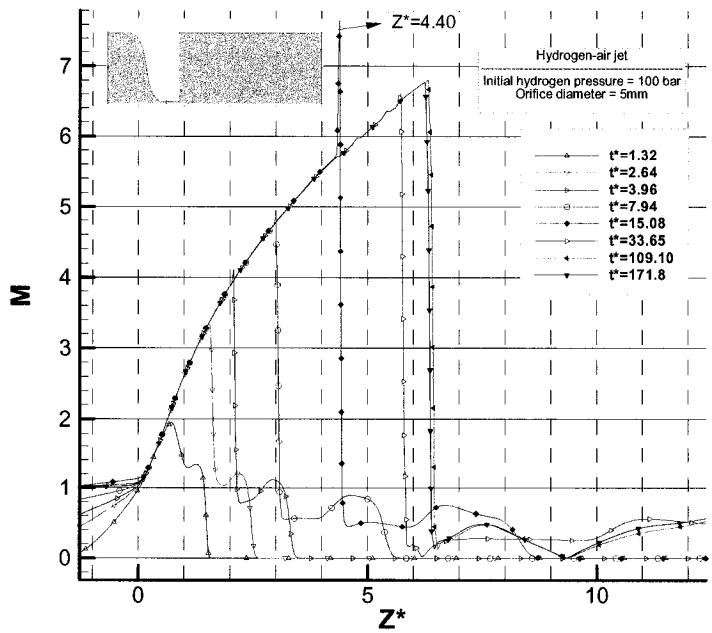

Figure 3.21 Distribution of Mach number along hydrogen-air jet axis

3.6.4 Density variation along the jet axis

The variations of the ratio of local density to the ambient density along the jet axis are shown in Figure 3.22 and Figure 3.23. The decrease and increase in density ratio graphs correspond to the passage of the fluid through the expansion and compression waves in the flow field. It is also clear from these graphs that in order to better capture the abrupt changes across the shock discontinuities the mesh grid has to be adapted according the flow conditions or an even finer mesh must be used.

3.6.5 Shear layer versus vortex ring

Formation of large and strong vortex rings in hydrogen-air jet is a distinctive feature of this flow which gives it a different configuration compared to hydrogen in hydrogen jet. In the case of hydrogen release into hydrogen, when flow becomes steady a long shear or mixing layer will forms which extends along the jet axis as can be seen in Figure 3.19. But when hydrogen is released into the air medium a very large vortex ring will be produced instead of the shear layer. This is because of the higher density of the air in comparison with hydrogen which does not allow the mixing layer to advance further downstream but rather push it toward the lateral sides so that it finally turns into a large vortex ring. This can be better understood during the evolution of hydrogen concentration field contours in section 3.7.2 of the present chapter.

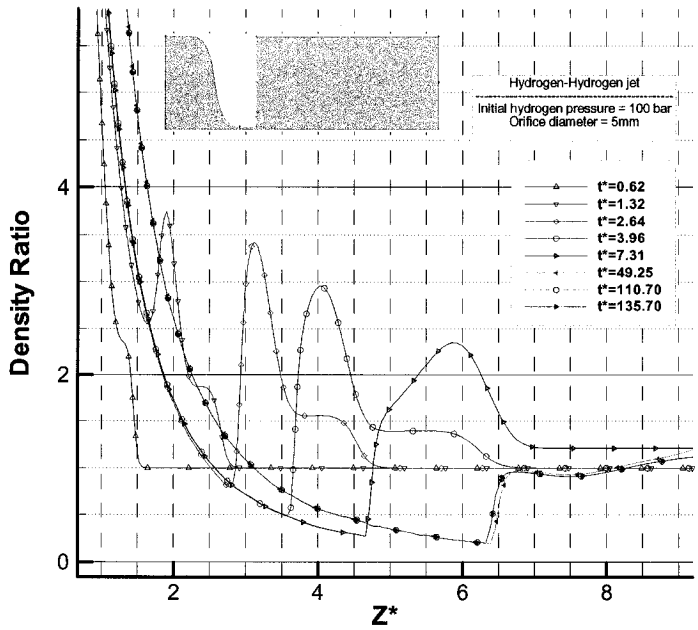

Figure 3.22 Local to far-field density ratio along the axis hydrogen-hydrogen jet

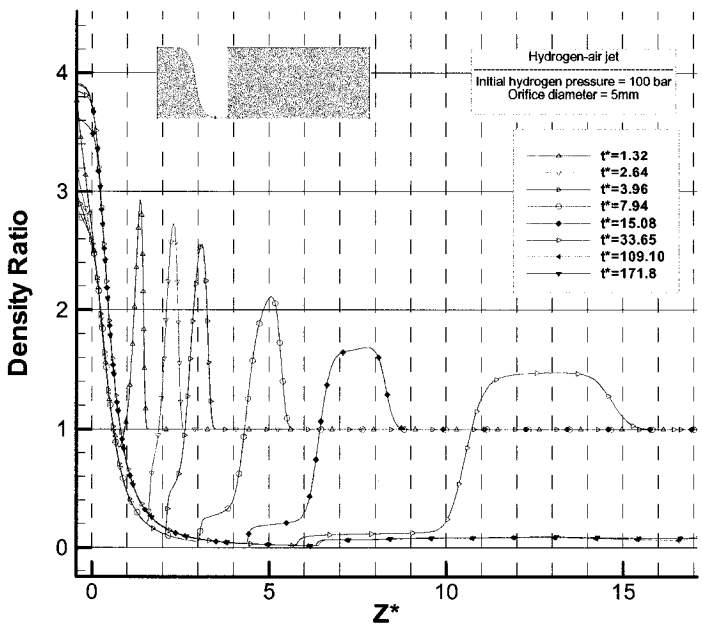

Figure 3.23 Local to far-field density ratio along the axis of hydrogen-air jet.

3.7 Simulation of 800-bar H_2-air jet

As it is discussed in section 1.2 of chapter 1, in order to have a reasonable fuel range when the vehicle is running on hydrogen compared to common fossil fuels, hydrogen potentially might need to be stored at much higher pressures. In this part of the thesis we are going to simulate the hydrogen jet from an 800-bar pressure vessel. The geometry and initial conditions which are used in this simulation are the same as those used in the simulation of hydrogen jet from the 100-bar reservoir presented in section 3.6 of the current chapter except the stagnation pressure inside the hydrogen tank which is 800 bars.

3.7.1 Analysis along the jet axis

The graphs for Mach number distribution along the jet center are shown in Figure 3.24 for different times during the hydrogen release. As it can be seen in this figure the final (settled) location of Mach disk is approximately at Z*=14.8 which corresponds to non-dimensional time of 110.90. The Mach number just before the Mach disk is about 9 and immediately after the shock goes to low subsonic level.

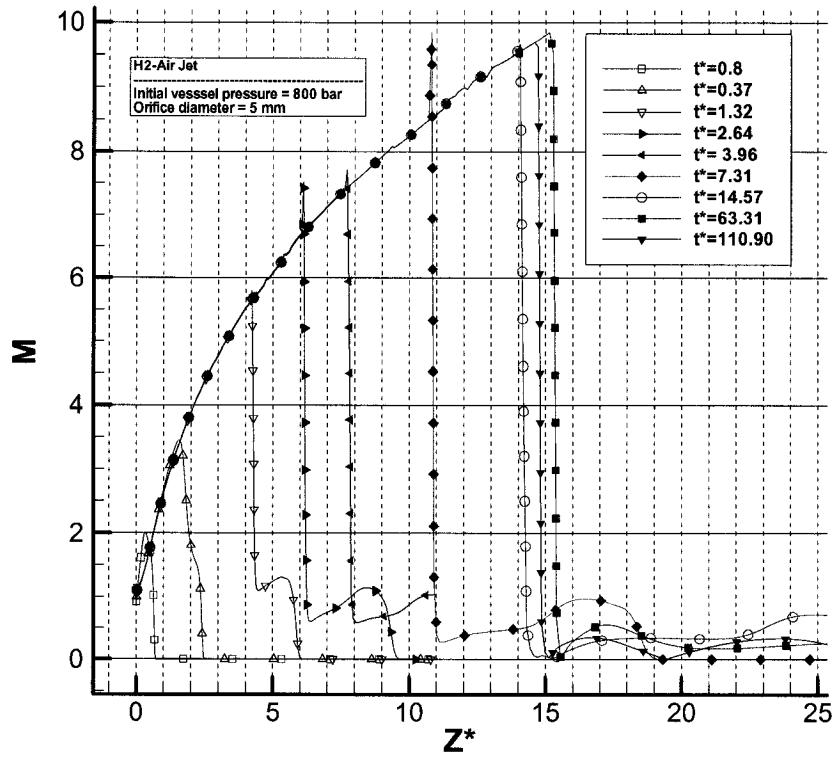

Figure 3.24 Mach number distribution along the centerline of the jet at several moments during the jet evolution after hydrogen release from an 800-bar pressure vessel.

After reaching to Z* of around 15.5 at t*=63.31 the Mach disk moves a little backward and settles at its final position as mentioned above. This backward movement of the Mach disk also is observed at the 100-bar pressure hydrogen jet (see Figure 3.21) and might be due to transient effects during the jet start-up. The overshoots which are discussed in section 3.5 are also observed in this simulation. The estimated values for Mach disk location and diameter based on the relationships 3.1 and 3.2 are 18.95 and 6.79. Compared to 100-bar jet which is discussed in section 3.6 the analytical values are

quite different from the corresponding results from present CFD simulation which are Z* of 14.8 and Mach disk diameter of approximately 4 as can be seen in Figure 3. 32.

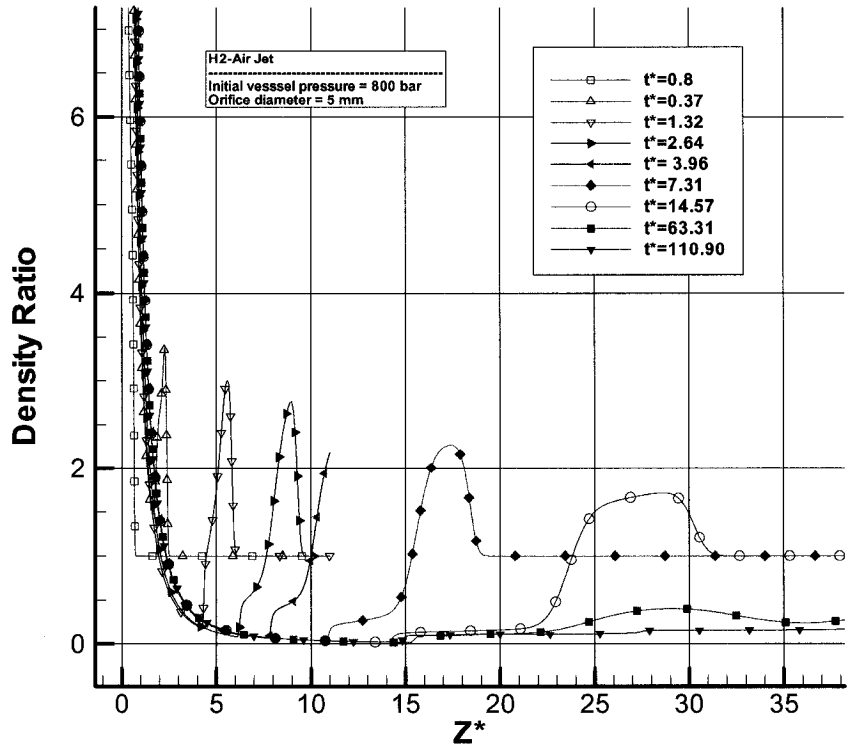

Figure 3.25 Density ratio along the axis of 800-bar hydrogen jet

The variations of ratio of local density to the room air density are shown in the Figure 3.25. It is evident from this figure that the shocks' strength are not captured very well and a mesh adaptation technique has to be applied in order to simulate the shocks more accurately. The Mach number contours at different times during the evolution of the 800-bar hydrogen jet are shown in Figure 3. 26 to Figure 3. 32. As it can be seen in these figures the hydrogen jet progress is much faster and stronger compared to 100-

bar jet previously reported in section 3.6. For example at t*=2.64 the Mach disk of the 100-bar hydrogen jet, Figure 3.10, is located at Z*=1.6 with the maximum Mach number of 3.4 while for the same time the Mach disk for the 800-bar jet is approximately at Z* of 6.2 with the Mach number of 7.6. Also it can be seen in Figure 3. 32 that as in the 100-bar hydrogen-air jet a vortex ring is formed after the Mach disk instead of mixing layer previously observed in hydrogen-hydrogen jet in section 3.6.

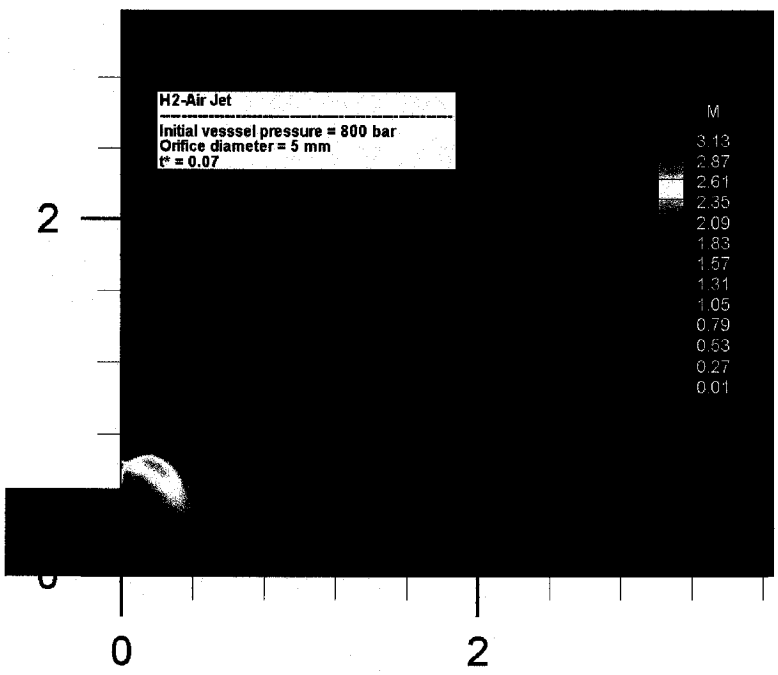

Figure 3. 26 Mach number contours in 800-bar hydrogen-air jet at t*= 0.07

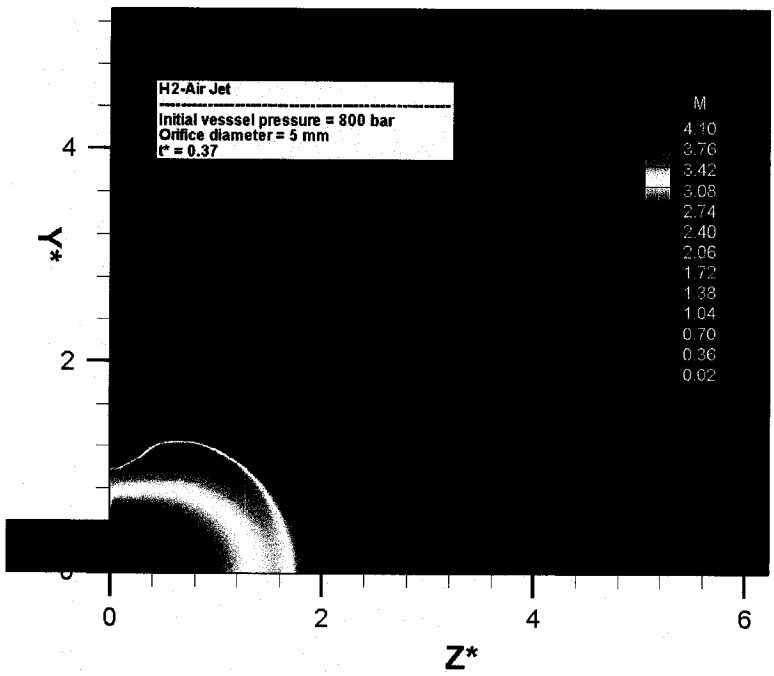

Figure 3. 27 Mach number contours in 800-bar hydrogen-air jet at t*= 0.37

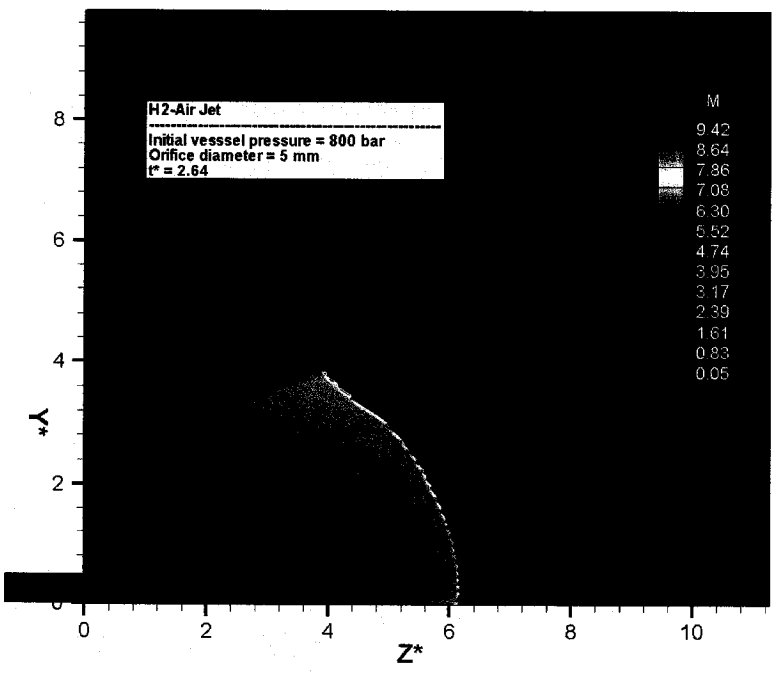

Figure 3. 28 Mach number contours in 800-bar hydrogen-air jet at t*= 2.64

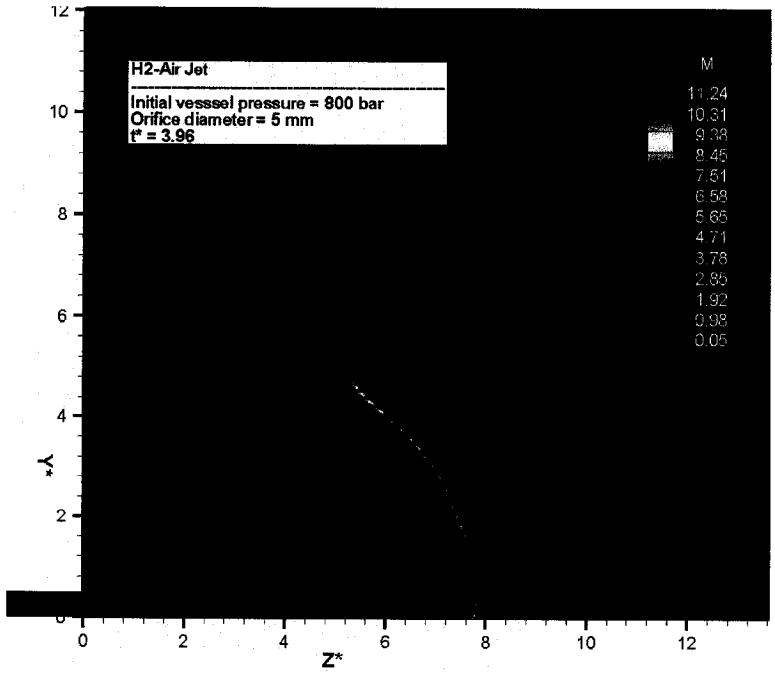

Figure 3. 29 Mach number contours in 800-bar hydrogen-air jet at t*= 3.96

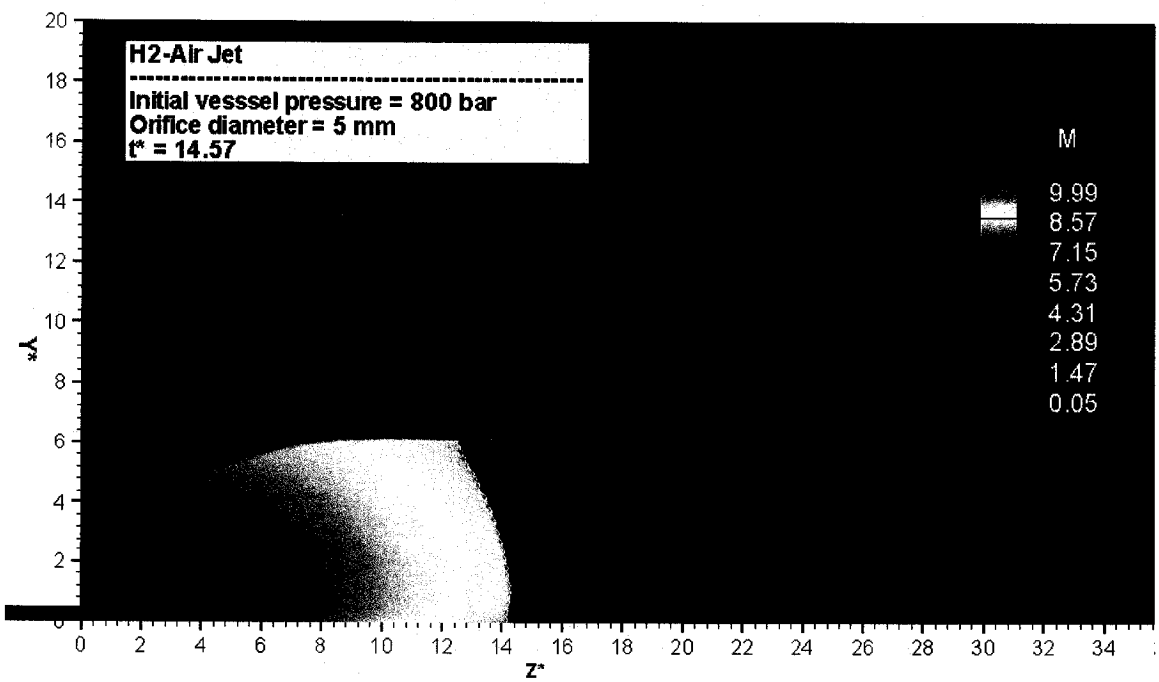

Figure 3. 30 Mach number contours in 800-bar hydrogen-air jet at t*= 14.57

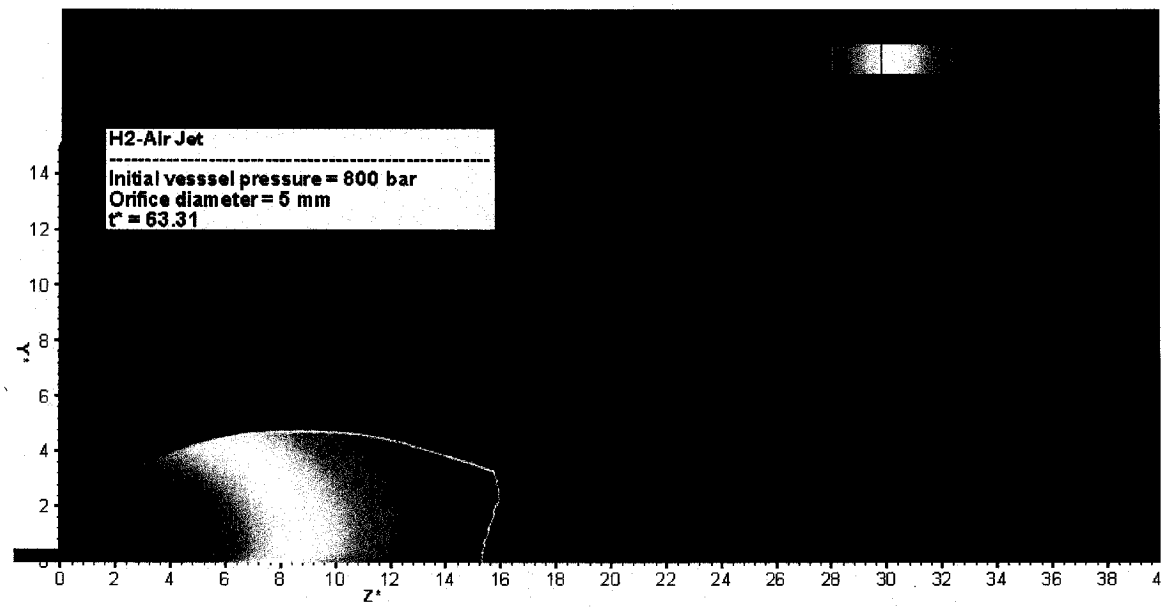

Figure 3. 31 Mach number contours in 800-bar hydrogen-air jet at t*= 63.31

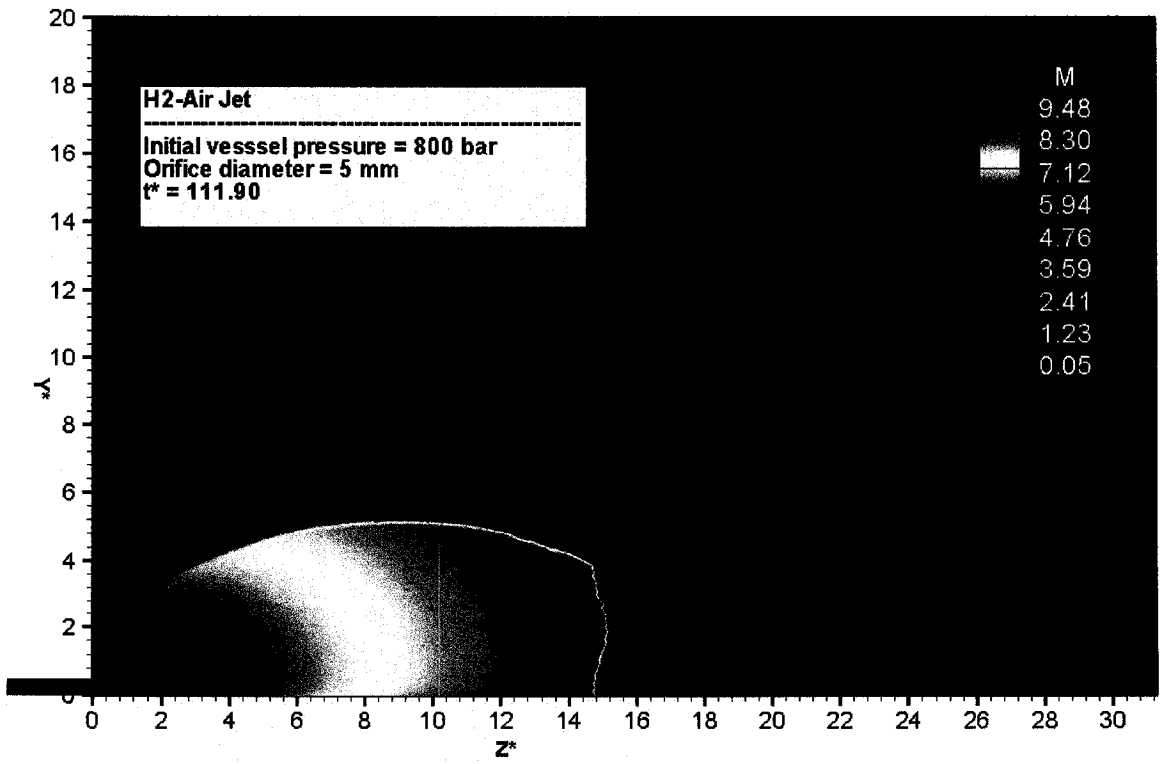

Figure 3. 32 Mach number contours in 800-bar hydrogen-air jet at t*= 111.90

3.7.2 Evolution of hydrogen concentration field at 800-bar H_2 release

The evolution of hydrogen concentration field is shown in Figure 3.33 to Figure 3.39. The hydrogen cloud grows with the hydrogen jet as the Mach disk moves toward its quasi-steady location along the jet axis and stays over there as long as the supply pressure is high enough. Nevertheless, the hydrogen concentration field never stops and continues its growth in the flow field as it is evident from Figure 3.33 to Figure 3.39. An important point which needs to be discussed in hydrogen concentration contours is the interface between hydrogen gas and the air.

Since we are assuming the inviscid flow and have ignored the diffusion term in the hydrogen species conservation equation we expect a sharp interface between two gases. However, it is clear from Figure 3.33 to Figure 3.39 that there is actually some diffusion happening along the interface of hydrogen and air. This in fact is the numerical diffusion which happens in the solution due to the numerical scheme. The unstructured tetrahedral elements which are used in this simulation are also responsible for this diffusive effect. By applying a mesh adaptation technique the numerical diffusion can be considerably reduced.

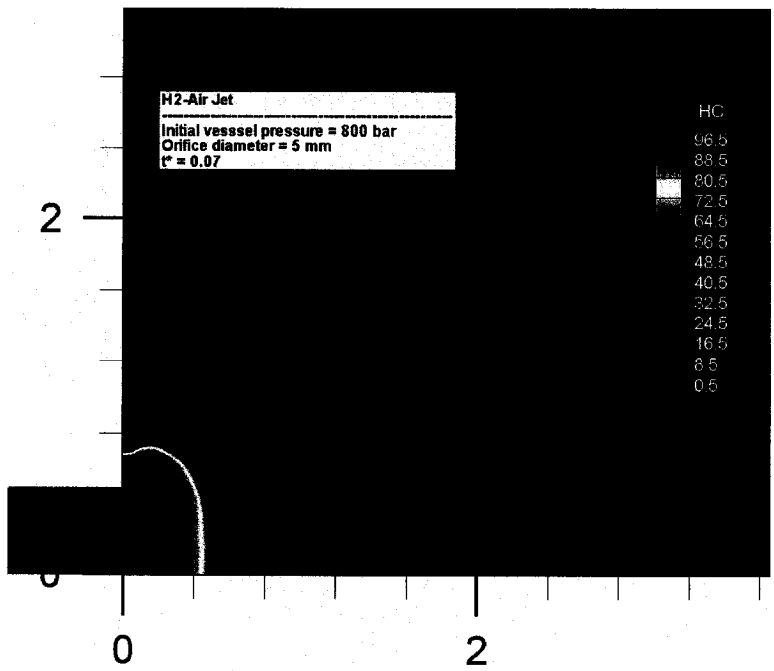

Figure 3.33 Hydrogen concentration field in 800-bar hydrogen-air jet, t=0.07(non-dim.)

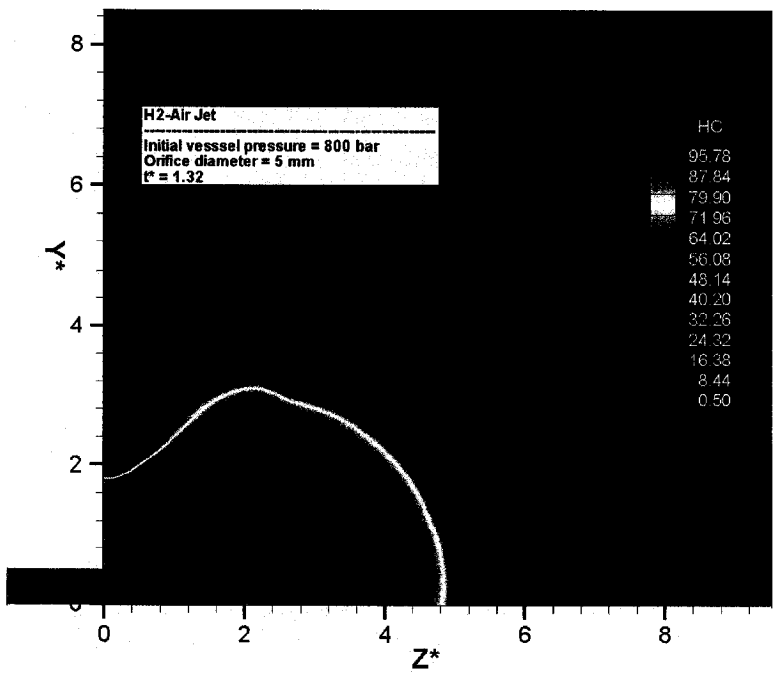

Figure 3. 34 Hydrogen concentration field in 800-bar hydrogen-air jet, t=1.32(non-dim.)

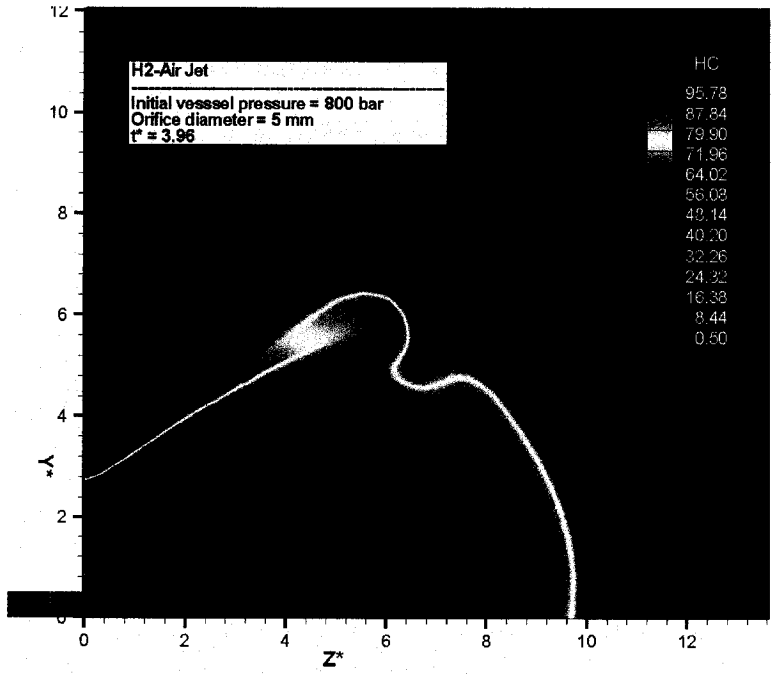

Figure 3. 35 Hydrogen concentration field in 800-bar hydrogen-air jet, t=3.96(non-dim.)

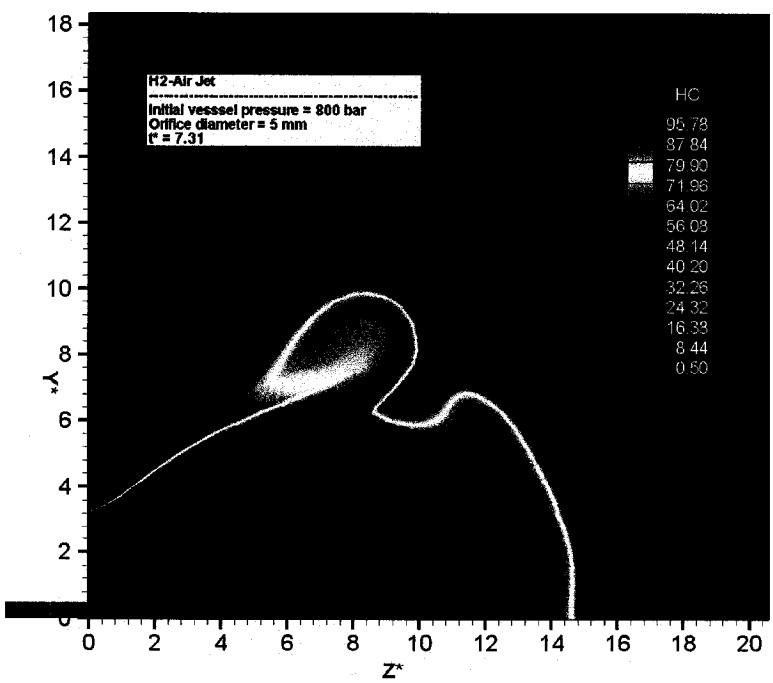

Figure 3. 36 Hydrogen concentration field in 800-bar hydrogen-air jet, t=7.31(non-dim.)

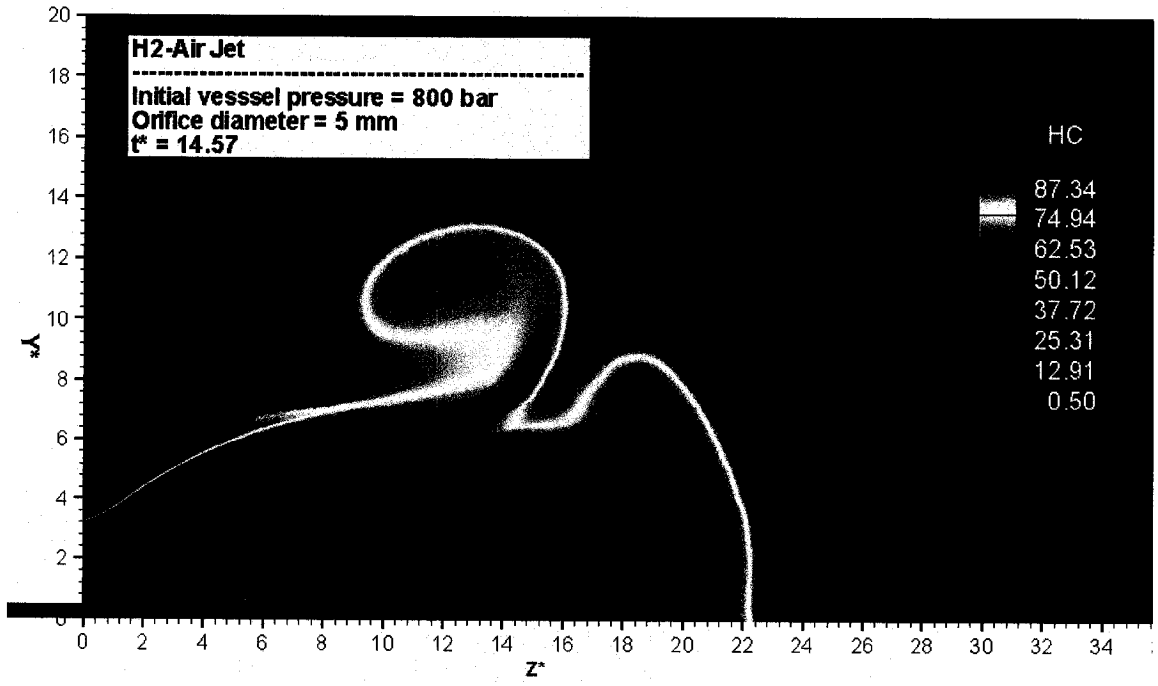

Figure 3. 37 Hydrogen concentration field in 800-bar hydrogen-air jet, t=14.57(non-dim.)

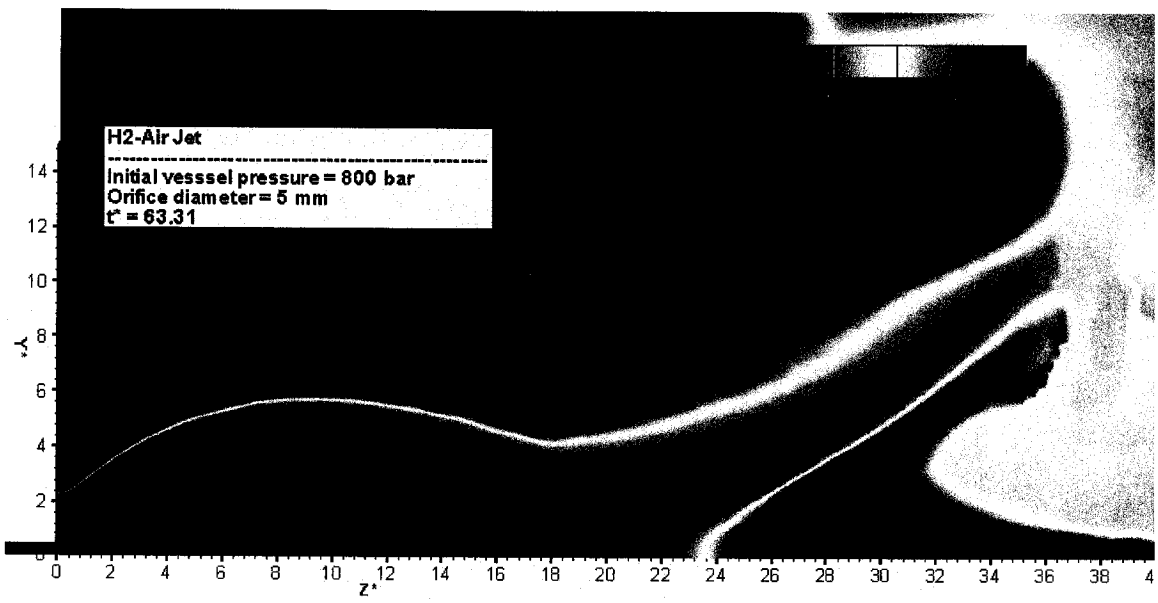

Figure 3. 38 Hydrogen concentration field in 800-bar hydrogen-air jet, t=63.31(non-dim.)

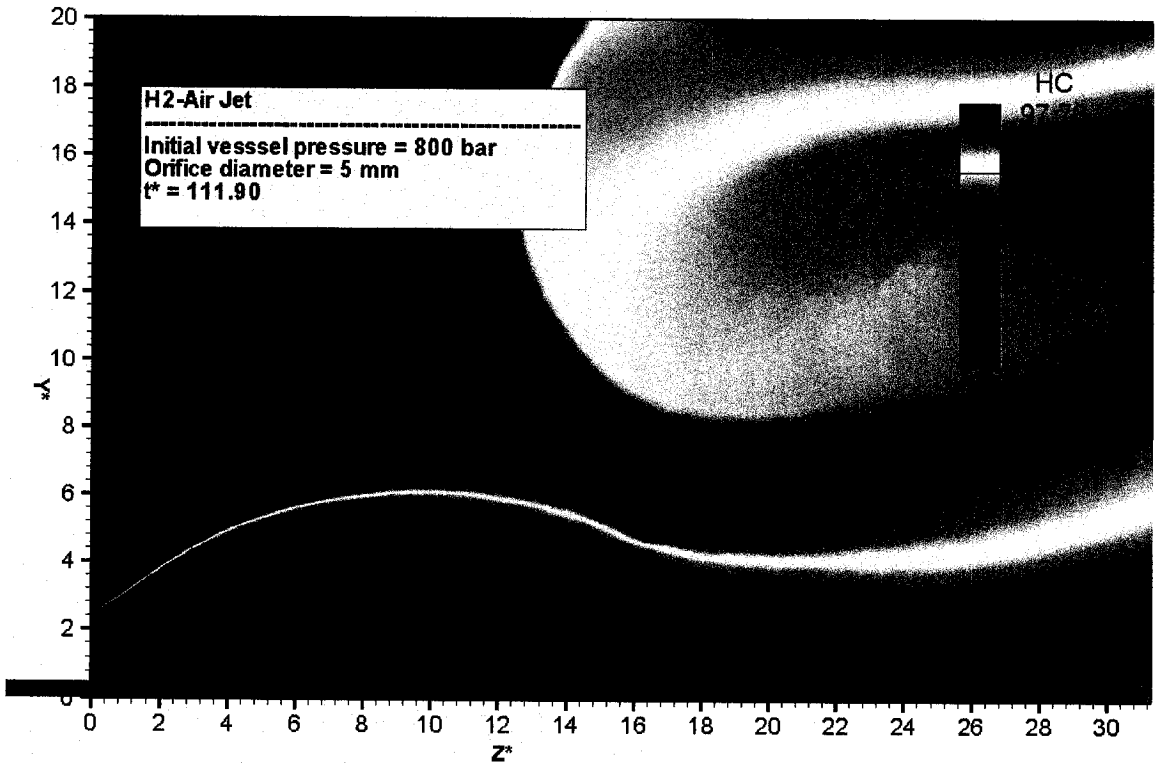

Figure 3.39 Hydrogen concentration field in 800-bar hydrogen-air jet, t=111.90(non-dim.)

3.7.3 Analysis in the vertical direction

In order to see the effects of numerical diffusion at the interface of two gases (hydrogen and air) the vertical distribution of flow variables are shown in Figures 3.40 to 3.42 for three positions along the jet axis. As it can be seen in Figure 3.40 at Z* = 4 there are strong oscillations happening at the interface of two gases which corresponds to jet boundary at that position along the jet axis. These oscillations are clearer in the temperature distribution graph in Figure 3.41.

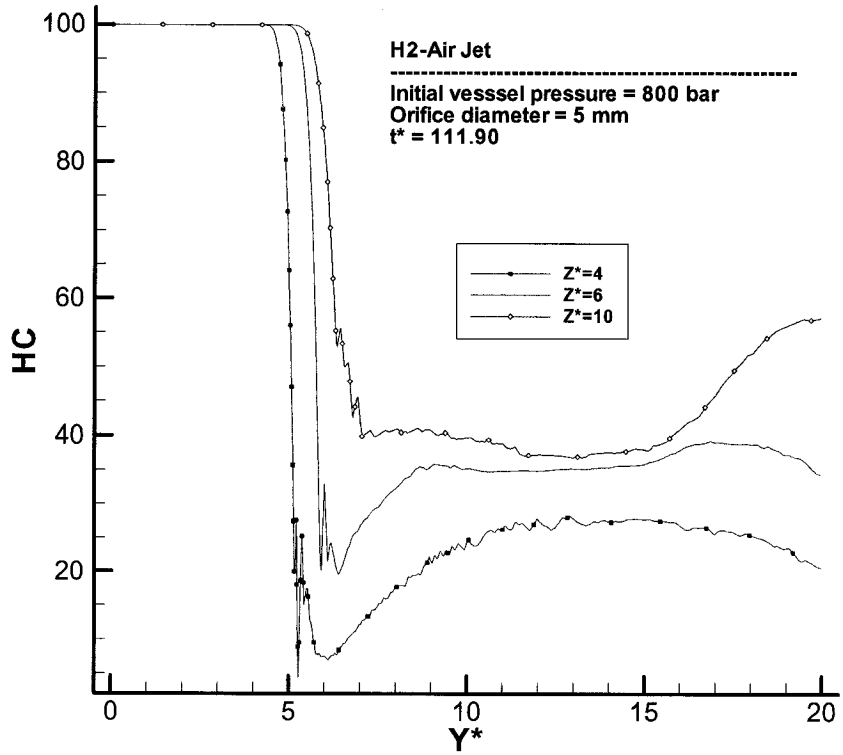

Figure 3.40 Vertical distribution of hydrogen concentration (%) at different positions along the jet axis

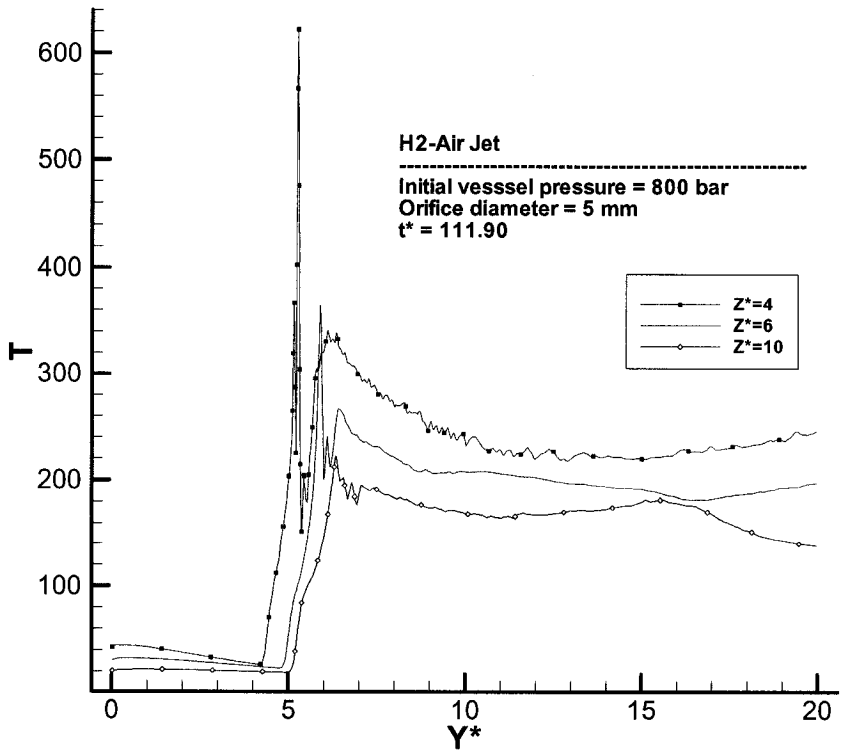

Figure 3.41 Vertical distribution of temperature (K) at different positions along the jet axis

As we go forward toward the Mach disk the oscillations at the interface of two gases decrease. This is due to the larger size of the region between barrel shock and the jet boundary as can be seen in Figure 3. 32. Although the numerical oscillations in the hydrogen concentration field are the cause of sharp picks in the temperature distribution, due to the natural interactions between the compression and expansion shock waves in the tiny region between the jet boundary and the barrel shock (as can be seen in Figure 2.2) still there might be real rise in the temperature field in that region. Hence, in order to accurately determine the temperature field first the numerical diffusions have to be reduced. This can be done by dynamically adapting the mesh grids and also by implementing the second-order accurate flux calculation schemes.

In order to see how the pressure is changing in the vertical direction the pressure variations in the vertical direction are shown in Figure 3.42 at three positions along the jet axis. As it can be seen in these graphs, the pressure is very low inside the barrel shock but immediately after the jet boundary it increases to the ambient pressure.

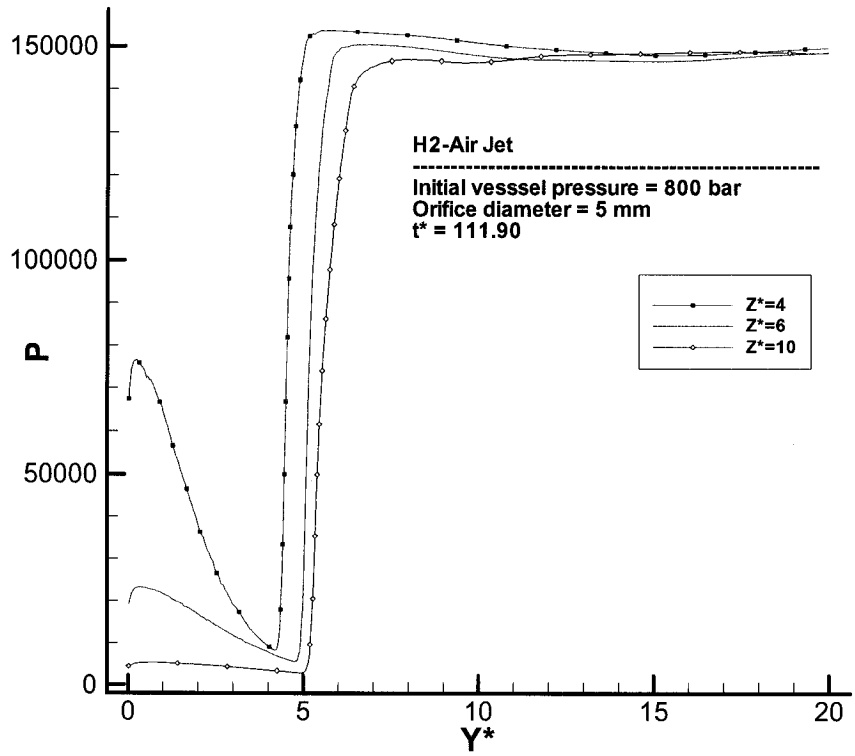

Figure 3.42 Vertical distribution of pressure (Pa) at different positions along the jet axis

4

Conclusions and Future works

In this chapter,

based on the outcomes of the performed numerical simulation some conclusions are made. In addition, some future works are suggested for further research and studies on this subject.

4.1 Conclusions

The highly under-expanded jets of hydrogen exiting high-pressure reservoir are studied. The effects of different medium into which the hydrogen is released are also analyzed in this thesis. In addition, the goal of simulation of hydrogen jet from an 800-bar pressure vessel is successfully achieved. The contributions which are made through this thesis can be listed as follows:

- ✓ Extension of an existing in-house compressible conservative Euler solver for solution of another transport equation for species conservation
- ✓ Parallelization of the subroutines which are added to the core solver by using MPI standard
- ✓ Validation of the code
- ✓ Simulation of hydrogen-air jet emanating from an 800-bar pressure storage tank

4.2 Future works

The following subjects are suggested as the future works:

- ➢ Real gas effects

As it is shown by Mohamed et al., [26], that the flow conditions at the exit of the orifice is significantly different when assuming hydrogen to be a real gas rather than an ideal gas. Consequently, this can considerably influence the downstream flow field. Hence, a study of real gas effects is necessary for better understanding of hydrogen release phenomenon.

- Higher order approximations

  The higher order flux approximations can reduce the numerical diffusions. It also helps to reduce of the computational power needed for simulations. As discussed in section 3.4.2 the numerical oscillations are the main obstacle in applying higher order flux calculation schemes. Therefore, implementation of a good limiter can resolve this issue.

- Dynamic mesh adaptation

  As it is mentioned, applying a mesh adaptation technique is quite necessary for simulation of highly underexpanded jets. It can significantly increase the accuracy of the results while reducing the computational power needed for such analysis.

- CFL optimization

  The rapid evolution of the highly underexpanded jets requires small linearized time steps during the early moments of the release process.

When the shock structures near the release point get settled the near-field flow resembles a quasi-steady flow which can be solved by using larger time steps. This condition remains valid as long as there is enough upstream pressure supply. Once the supply pressure drops below highly underexpanded level the rapid changes in the flow field begin to reappear and again require small time steps to be accurately captured. Applying an optimization method which is able to adjust the CFL value according to different period of the release can considerably increase the simulation speed.

- Turbulence modeling

  Extension to the Navier-Stokes equations and finding an appropriate turbulence model for highly underexpanded hydrogen jet is also very important particularly when we are interested in studying of the concentration field in the entire room space.

References

[1]. Module 1: Hydrogen Properties, College of Deseret, Revision 0, December 2001.

[2]. P. Birkby, and G.J. Page, Numerical predictions of turbulent underexpanded sonic jets using a pressure-based methodology, Proc. Instn. Mech. Engrs., Vol 215, part G, 2001.

[3]. T.S. Cheng, and K.S. Lee, Numerical simulation of underexpanded supersonic jet and free shear layer using WENO schemes, International Journal of Heat and Fluid Flow, vol. 26, 755-770, 2005.

[4]. S.G. Cheuch, M.C. Lai, and G.M. Faeth, Structure of turbulent sonic underexpanded free jets, AIAA J., Vol. 27, 549-559, 1989.

[5]. J.A. Wilkes, C.E. Glass, P.M. Danehy, and R.J. Nowak, Fluorescence Imaging of Underexpanded Jets and Comparison with CFD, AIAA paper, 2006-0910, 2006.

[6]. T.C. Adamson, and J.A. Nicholls, Final Report on the Structure of Jets from Highly underexpanded Nozzles into Still Air, Engineering Research Institute, University of Michigan Ann Arbor, Feb. 1958.

[7]. A.Yu. Gostintsev, V.V. Zelentsov, V.S. Ilyukhin, and P.F. Pokhil, Structure of Underexpanded Supersonic Swirling Jet, Izv. An SSSR, Mekhanika Zhidkosti I Gaza, vol.4, No. 5, pp. 158-162, 1969.

[8]. A.D. Birch, D.R. Brown, D.K. Cook, and G.K. Hargrave, Flame Stability in Underexpanded Natural Gas Jets, Combustion Sci. and Tech., vol. 58, pp. 267-280, 1988.

[9]. A.V. Emel 'yanov, and A.V. Eremin, Generalized Empirical Laws of Starting Discontinuity Dynamics Associated with the Startup of Underexpanded Jets, Zhurnal Prikladnoi I Tekhnicheskoi Fiziki, No. 5, pp. 22-26, 1991.

[10]. V.V. Golub, Development of shock wave and vortex structures in unsteady jets, Shock Waves, 3:279-285, 1994.

[11]. T.V.R. Rao, R.R. Kumar, and J. Kurian, Near Field Shock Structure of Dual Co-axial Jets, Shock Waves, 6:361-366, 1996.

[12]. R. Ishii, H. Fujimotot, N. Hatta, and Y. Umeda, Experiemntal and Numerical Analysis of Circular Pulse Jets, J. of Fluid Mechanics, vol. 392, pp. 129-153, 1999.

[13]. C.B. Devaud, J.B. Kelman, J.B. Moss, and C.D. Stewart, Stability of Underexpanded Supersonic Jet Flames Burning H_2-CO, Shock Waves, 12:241-249, 2002.

[14]. M. Rahimi, I. Owen, and J. Mistry, Heat Transfer Between an Underexpanded Jet and a Cylinderical Surface, International J. of Heat and Mass Transfer, vol. 46, 3135-3142, 2003.

[15]. Takao Suzuki, and Sanjiva K. Lele, Shock Leakage through an Unsteady Vortex-laden Mixing Layer: Application to Screech Jet, J. of Fluid Mechanics, vol. 490, pp. 139-167, 2003.

[16]. Y. Li, A. Kirkpatrick, C. Mitchell, and B. Willson, Characteristic and Computational Fluid Dynamics Modeling of High-Pressure Gas Jet Injection, ASME J. of Engineering for Gas Turbines and Power, vol. 126, pp. 192-197, 2004.

[17]. M. Belan, S. De Ponte, and S. Massaglia, Experiments and Numerical Simulations on the Mid-Term Evolution of Hypersonic Jets, Astrophysics and Space Science, 293:225-232, 2004.

[18]. I.O. Sand, K. Sjoen, and J.R. Bakke, Modeling of Release of Gas from High-Pressure Pipelines, International J. for Numerical Methods in Fluids, vol. 23, 953-983, 1996.

[19]. W. Breitung, G. Necker, B. Kaup, and A. Veser, Numerical Simulation of Hydrogen Release in a Private Garage, proceedings of Hypothesis IV, p. 368, Strahlsund, Germany, 9-14 September 2001.

[20]. A.G. Venetsanos, T. Huld, P. Adams, and J.G. Bartzis, Source, dispesion and combustion modeling of an accidental release of hydrogen in an urban environment, Journal of Hazardous Material, A105, 1-25, 2003.

[21]. Vladimir Agranat, Zhong Cheng, and Andrei Tchouvelev, CFD Modelling of Hydrogen Release and Dispersion in Hydrogen Energy Station, Stuart Energy Systems Corporation, Mississauga, Canada, 2004.

[22]. B. Angers, A. Hourri, P. Benard, P. Tessier, et al., Simulation of Hydrogen Release from a Storage Tank: Dispersin and Consequences of Ignition, The Fisrt International Conference on Hydrogen Safety, Pisa, Italy, Sep. 8-10, 2005.

[23]. H. Wilkening, and D. Baraldi, CFD Modelling of Accidental Hydrogen Release from Pipelines, The Fisrt International Conference on Hydrogen Safety, Pisa, Italy, Sep. 8-10, 2005.

[24]. S. Mukai, J. Suzuki, H. Mitsuishi, K. Oyakawa, and S. Watanabe, CFD Simulation of Hydrogen Leakage Caused by Fuel Cell Vehicle Accident in Tunnel, Underground Parking Lot and Multistory Parking Garage, Japan Automobile Research Institue, vol. 27, No. 29, 2005.

[25]. G. Pedro, F. Peneau, P. Oshkai, and N. Djilali, Computational Analysis of Transient Gas Release from a High Pressure Vessel,.

[26]. K. Mohamed, and M. Paraschivoiu, Real gas simulation of hydrogen release from a high-pressure chamber, International journal of hydrogen energy, vol. 30, no8, pp. 903-912, 2005.

[27]. M. Jugroot, C.P.T. Groth, B.A. Thomson, V. Baranov, and B. Collings, Numerical investigation of interface region flows in mass spectrometers: neutral gas transport, Jornal of Physics D: Applied Physics, vol.37, pp. 1289-1300, 2004.

[28]. J.M. Seiner, T.D. Norum, Experiments of shock associated noise on supersonic jets, AIAA paper 79-1526, 1979.

[29]. J.M. Seiner, T.D. Norum, Aerodunamic aspects of shock containing jet plumes, AIAA 80-0965, 1980.

[30]. J.K. Prasad, R.C. Mehta, and R.C. Sreekanth, Impingement of supersonic jets on an axissymmetric deflector, AIAA Journal 32, 1535-1538.

[31]. S.M. Dash, D.E. Wolf, and J.M. Seiner, Analysis of turbulent underexpanded jets, part I: parabolized Navier-tokes model, SCIPVIS, AIAA Journal 23, 505-514, 1985.

[32]. C.-M. Ho, L.-S. Huang, Subharmonics and vortex merging in mixing layers, Journal of Fluid Mechanics 119, 443-473, 1982.

[33]. F.F. Grinstein, E.S. Oran, and J.P. Boris, Numerical simulation of asymmetric mixing in planar shear flows, Journal of Fluid Mechanics 165, 201-220, 1986.

[34]. J.D. Ramshaw, Fluid dynamics and energetic in ideal gas mixtures, Am. J. Phys. 70 (5), 2002.

[35]. P. Jenny, B. Muller, and H. Thomann, Correction of Conservative Euler Solver for Gas Mixtures, Journal of Computational Physics 132, 91-107, 1997.

[36]. C.J. Ho, A continuum model for transport phenomena in a convective flow of solid-liquid phase change material suspensions, Applied Mathematical Modeling 29, 805-817, 2005.

[37]. L. Hallo, C. Le Ribault, M. Buffat, An Implicit Mixed Finite-Volume-Finite-Element Method for Solving 3D Turbulent Compressible Flows, Intl. J. for Numerical Methods in Fluids, vol.25, 1241-1261, 1997.

[38]. C. Hirtsch, "Numerical Computation of Internal and External Flows", vol. 2, John Wiley & Sons, 1990.

[39]. P. Jawahar, H. Kamath, A High-Resolution Procedure for Euler and Navier-Stokes Computations on Unstructured Grids, Journal of Computational Physics 164, 165-203, 2000.

[40]. S. Tu, S. Aliabadi, A Slope Limiting Procedure in Discontinuous Galerkin Finite Element Method for Gasdynamics Applications, International Journal of Numerical Modeling and Analysis, vol. 2, No. 2, pp. 163-178, 2005.

[41]. L. Cueto-Felgueroso, I. Colominas, F. Navarrina, and M. Casteleiro, Finite volume solvers and moving least-squares approximations for the compressible Navier-Stokes

equations on unstructured grids, Computer methods in applied mechanics and engineering, May 26, 2005.

[42]. W.S Young, Derivation of the free-jet Mach-disk location using the entropy-balance principle, Physics of Fluids, vol. 18, p. 1421-1425, Nov. 1975.

[43]. H. Ashkenas, F.S. Sherman, The Structure and Utilization of Supersonic Free Jets in Low Density Wind Tunnel, Rarefied Gas Dynamics, Fourth Symposium, vol. II, Academic, New York, pp. 84-105, 1966.

[44]. S. Cris, P.M. Sherman, D.R. Glass, Study of Highly Under-Expanded Sonic Jet, AIAA J., 4, pp. 68-71, 1966.

[45]. Fluent User Guide, Section 14.1.1, 2005.

[46]. S. Yu, Y.-L. Peter Tsai, and J. SHuen, Three-Dimensional Calculations of Supersonic Reacting Flow Using an LU Scheme, Journal of Computational Physics 101, 276-286, 1992.

A.1. Navier-Stokes equations for mixture

The Navier-Stokes extension of the Euler solver discussed in the main text of this thesis is presented here. If the velocity field is assumed to be the mass-averaged velocity (as discussed in the section 2.2 of the main text), then the N-S equations remain almost the same as for a pure fluid:

$$\frac{\partial \rho}{\partial t} + \vec{\nabla} \cdot (\rho \vec{V}) = 0 \qquad \text{A. 1}$$

$$\frac{\partial (\rho \vec{V})}{\partial t} + \vec{\nabla} \cdot (\rho \vec{V} \otimes \vec{V} + p\bar{\bar{I}} - \bar{\bar{\tau}}) = \rho \vec{g} \qquad \text{A. 2}$$

$$\frac{\partial (\rho E)}{\partial t} + \vec{\nabla} \cdot (\rho \vec{V} H - k\vec{\nabla} T - \rho \sum_{i=1}^{2} h_i D_{im} \vec{\nabla} C_i - \bar{\bar{\tau}} \cdot \vec{V}) = \rho \vec{g} \cdot \vec{V} \qquad \text{A. 3}$$

with,

$$\tau_{ij} = \mu[(\partial_j v_i + \partial_i v_j) - \tfrac{2}{3}(\vec{\nabla} \cdot \vec{V})\delta_{ij}] \qquad \text{A. 4}$$

$$H = h + \tfrac{1}{2}V^2 \qquad \text{A. 5}$$

$$h = e + p/\rho \qquad \text{A. 6}$$

$$E = e + \tfrac{1}{2}V^2 \qquad \text{A. 7}$$

The diffusion term in the energy equation represents transport of enthalpy due to species diffusion. This term in many multi-component gas flows can have a significant effect, particularly when the Lewis number:

$$Le_i = \frac{k}{\rho c_p D_{i,m}} \qquad \text{A. 8}$$

for any species is far from unity and neglecting it can lead to significant errors, [45]. This is actually the case for Hydrogen with $Le = 2.5$ at atmospheric conditions. The binary diffusion coefficient $D_{i,m}$ can be calculated from the following relationships, [45,46].

$$D_{im} = \frac{(1 - X_i)}{\sum_{i \neq j} \frac{X_i}{D_{ij}}} \qquad \text{A. 9}$$

$$X_i = \frac{C_i / M_i}{\sum_{j=1}^{2} C_j / M_j} \qquad \text{A. 10}$$

A.2. Species conservation equation

In the above N-S equations for the gas mixture there are seven unknowns and six equations, hence another relationship is required to close this system of equations. This

equation is the species conservation equation through which transportation of mixture component is modeled.

$$\frac{\partial(\rho C_a)}{\partial t} + \vec{\nabla} \cdot (\rho C_a \vec{V}) = \vec{\nabla} \cdot (\rho D_C \vec{\nabla} C_a) \qquad \text{A. 11}$$

In order to minimize the numerical error, equation A. 11 is written for the major component of the mixture which in the present case is the air mass fraction C_a. Hydrogen mass fraction then can be easily determined from equation A. 12.

$$C_a + C_h = 1 \qquad \text{A. 12}$$

A.3. Numerical discretization

The numerical methods which are used in this research are based on an implicit mixed finite element-finite volume scheme, [37]. According to this scheme, finite element technique is used for all diffusive and source terms, while for temporal and convective terms finite volume method is applied. Figure 2.3 shows a two dimensional schematics of finite elements and finite volumes used in numerical integration of the governing equations. As it is shown in this figure different shape functions are used for finite elements and finite volumes. For finite elements the shape function linearly varies

from one at node i to zero at the element boundaries, while for finite volumes the shape is one all over the control volume and zero everywhere else.

- **Discretization of the diffusion term in the species transport equation**

In order to discretize the species transport equation a weak formulation is written as follows:

$$\int_{\Omega} \frac{\partial(\rho C_a)}{\partial t} \psi \, d\sigma + \int_{\Omega} \vec{\nabla} \cdot (\rho C_a \vec{V}) \psi d\sigma = \frac{1}{\mathrm{Re}\, Sc} \int_{\Omega} \vec{\nabla} \cdot (\rho D_C \vec{\nabla} C_a) \psi \, d\sigma \qquad \text{A. 13}$$

Where, ψ is the test function and is the same as shape function. Using the hybrid finite volume-finite element discretization scheme, this test function corresponds to ϕ_i for finite elements and ψ_i for finite volumes. Hence the equation A. 13 can be written in the following form.

$$\int_{\Pi_i} \frac{\partial(\rho C_a)}{\partial t} d\sigma + \int_{\Pi_i} \vec{\nabla} \cdot (\rho C_a \vec{V}) d\sigma = \frac{1}{\mathrm{Re}\, Sc} \int_{\Omega} \vec{\nabla} \cdot (\rho D_C \vec{\nabla} C_a) \psi_i \, d\sigma \qquad \text{A. 14}$$

Integration of the equation A. 14 for all nodes i in the domain of calculation, yields a linear system of equations which needs to be solved.

Diffusive term:

$$\int_{\Omega} \vec{\nabla} \cdot (\rho D_C \vec{\nabla} C_a) \psi_i \, d\sigma = D_i \overline{C}_a \qquad \text{A. 15}$$

Spatial discretization-Diffusive term:

As previously discussed, finite element method is used for the diffusion term. With this purpose, the diffusion term is first integrated by part.

$$D_i \overline{C}_a = \int_{\partial\Omega} \psi_i \, \rho D_C \vec{\nabla} C_a \cdot \vec{n} \, ds - \int_{\Omega} \rho D_C \vec{\nabla} C_a \cdot \vec{\nabla} \psi_i \, d\sigma \qquad \text{A. 16}$$

The surface integral term in the above equation is associated with the gradient of species mass fraction across the boundary. Since the computational domain in the problem of our interest is enclosed by solid surfaces and far fields and the mass fraction species across these boundaries is actually zero, this term can be neglected. Therefore, equation A. 16 is only left with the volume integral.

$$\begin{aligned} D_i \overline{C}_a &= -\int_{\Omega} \rho D_C \vec{\nabla} C_a \cdot \vec{\nabla} \psi_i \, d\sigma \\ &= -\sum_{e=1}^{E} \int_{\Omega_e} \rho D_C \vec{\nabla} C_a \cdot \vec{\nabla} \psi_i \, d\sigma \end{aligned} \qquad \text{A. 17}$$

where, $E \equiv$ Total number of finite elements

Now defining the following field variables,

$$\rho = \sum_j \rho_j \varphi_j \ , \ C_a = \sum_r C_{a_r} \quad \text{, and} \quad D_C = \sum_k D_{C_k} \varphi_k$$

the volume integral in equation A. 17 can be numerically integrated as follows:

$$\begin{aligned} \int_{\omega_e} \rho D_C \vec{\nabla} C_a \cdot \vec{\nabla} \psi_i \, d\sigma &= \int_{\omega_e} (\sum_j \rho_j \varphi_j)(\sum_k D_{C_k} \varphi_k) \vec{\nabla} \sum_r (C_{a_r} \varphi_r) \cdot \vec{\nabla} \psi_i \, d\sigma \\ &= \sum_j \sum_k \sum_r \rho_j D_{C_k} C_{a_r} \int_{\omega_e} \varphi_j \varphi_k \vec{\nabla} \varphi_r \cdot \vec{\nabla} \psi_i \, d\sigma \\ &= \sum_j \sum_k \sum_r \rho_j D_{C_k} C_{a_r} A_{r,i} M_{j,k} \end{aligned}$$

where,

$$A_{r,i} = \vec{\nabla} \varphi_r \cdot \vec{\nabla} \psi_i \quad \text{and} \quad M_{j,k} = \int_{\omega_e} \varphi_j \varphi_k \, d\sigma$$

- **Discretization of the enthalpy diffusion term**

As discussed in section A.1 a new term has to be added in the energy equation which represents variation of enthalpy due to diffusion of species mass fraction. This new term must be discretized order to be included to the system of the equations. Since this term is a diffusion term, it will be discretized by finite element techniques. Considering this new term it can be integrated in the following manner.

Using the ideal gas law it can be rewritten as,

$$\vec{\nabla}\cdot(\rho\sum_{j=1}^{2}h_j D_{jm}\vec{\nabla}C_j)=\vec{\nabla}\cdot(\rho T\sum_{j=1}^{2}c_{p_j}D_{jm}\vec{\nabla}C_j)$$
$$=\vec{\nabla}\cdot(\frac{p}{R_{gas}}\sum_{j=1}^{2}c_{p_j}D_{jm}\vec{\nabla}C_j)$$

Integrating in space yields,

$$\int_{\Omega_i}\vec{\nabla}\cdot(\frac{p}{R_{gas}}\sum_{j=1}^{2}c_{p_j}D_{jm}\vec{\nabla}C_j)\varphi_i d\sigma=\sum_{j=1}^{2}c_{p_j}\int_{\Omega_i}\vec{\nabla}\cdot(pY\vec{\nabla}C_j)\varphi_i d\sigma \qquad \text{A. 18}$$

with,

$$Y=\frac{D_{jm}}{R_{gas}}$$

Integrating by part,

$$\int_{\Omega_i}\vec{\nabla}\cdot(pY\vec{\nabla}C_j)\varphi_i d\sigma=\int_{\partial\Omega_i}\varphi_i pY\vec{\nabla}C_j\cdot\vec{n}ds-\int_{\Omega_i}pY\vec{\nabla}C_j\cdot\vec{\nabla}\varphi_i d\sigma \qquad \text{A. 19}$$

The surface integral in the above equation is again neglected as previously discussed for source term integration. Therefore the above equation becomes:

$$\int_{\Omega_i}\vec{\nabla}\cdot(pYD_{jm}\vec{\nabla}C_j)\varphi_i d\sigma=-\int_{\Omega_i}pY\vec{\nabla}C_j\cdot\vec{\nabla}\varphi_i d\sigma \qquad \text{A. 20}$$

Now defining the field variables,

$$p=\sum_{t=1}^{N} p_t\phi_t\,,\quad C_j=\sum_{q=1}^{N} C_{j_q}\psi_q\,,\quad Y=\sum_{l=1}^{N} Y_l\beta_l$$

Then the volume integral can be numerically integrated.

$$\int_{\Omega_i} pY\vec{\nabla}C_j\cdot\vec{\nabla}\varphi_i d\sigma=\sum_{e=1}^{E}\int_{\omega_e} pY\vec{\nabla}C_j\cdot\vec{\nabla}\varphi_i d\sigma$$

$$\begin{aligned}\int_{\omega_e} pY\vec{\nabla}C_j\cdot\vec{\nabla}\varphi_i d\sigma&=\int_{\omega_e}(\sum_t p_t\phi_t)(\sum_l Y_l\beta_l)\vec{\nabla}(\sum_q C_{j_q}\psi_q)\cdot\vec{\nabla}\varphi_i d\sigma\\&=\sum_t\sum_l\sum_q p_tY_lC_{j_q}\int_{\omega_e}\phi_t\beta_l\vec{\nabla}\psi_q\cdot\vec{\nabla}\varphi_i d\sigma\\&=\sum_t\sum_l\sum_q p_tY_lC_{j_q}\vec{\nabla}\psi_q\cdot\vec{\nabla}\varphi_i M^e_{t,l}\end{aligned}$$

with,

$$M^e_{t,l}=\int_{\omega_e}\phi_t\beta_l d\sigma$$

finally,

$$\int_{\Omega_i}\vec{\nabla}\cdot(\frac{p}{R_{gas}}\sum_{j=1}^{2} c_{p_j}D_{jm}\vec{\nabla}C_j)\varphi_i d\sigma=-\sum_{j=1}^{2}\sum_e\sum_t\sum_l\sum_q c_{p_j}p_tY_lC_{j_q}\vec{\nabla}\psi_q\cdot\vec{\nabla}\varphi_i M^e_{t,l}\qquad \text{A. 21}$$

Contribution to the Jacobian matrix:

In order to linearize the system of nonlinear N-S equations as discussed earlier, the contribution the enthalpy diffusion term to Jacobian matrix has to be determined. In

order to facilitate this procedure, first the diffusive flux 2.41 is rewritten in terms of conservative variables. First,

$$p_t = (\gamma - 1)(\rho E - \tfrac{1}{2}\rho^2 V^2 / \rho)$$

or,

$$p_t = (\gamma - 1)\left(\varepsilon - \tfrac{1}{2}(m^2 + n^2 + l^2)/\rho\right)$$

Equation 2.41 now can be written as:

$$Dflux = -\sum_{j=1}^{2}\sum_{e}\sum_{t}\sum_{l}\sum_{q} c_{p_j}\left[(\gamma - 1)\left(\varepsilon - \tfrac{1}{2}(m^2 + n^2 + l^2)/\rho\right)\right]_t Y_l C_{j_q} \vec{\nabla}\psi_q \cdot \vec{\nabla}\varphi_i M^e_{t,l} \quad \text{A. 22}$$

Taking the derivatives with respect to conservative variables, the following Jacobian terms will be obtained.

$$\frac{\partial Dflux}{\partial \rho} = -\sum_{j=1}^{2}\sum_{e}\sum_{l}\sum_{q} c_{p_j}\left[\tfrac{1}{2}(\gamma - 1)(m^2 + n^2 + l^2)/\rho^2\right]_t Y_l C_{j_q} \vec{\nabla}\psi_q \cdot \vec{\nabla}\varphi_i M^e_{t,l} \quad \text{A. 23}$$

$$\frac{\partial Dflux}{\partial m} = \sum_{j=1}^{2}\sum_{e}\sum_{l}\sum_{q} c_{p_j}\left[(\gamma - 1)m/\rho\right]_t Y_l C_{j_q} \vec{\nabla}\psi_q \cdot \vec{\nabla}\varphi_i M^e_{t,l} \quad \text{A. 24}$$

$$\frac{\partial Dflux}{\partial n} = \sum_{j=1}^{2}\sum_{e}\sum_{l}\sum_{q} c_{p_j}\left[(\gamma - 1)n/\rho\right]_t Y_l C_{j_q} \vec{\nabla}\psi_q \cdot \vec{\nabla}\varphi_i M^e_{t,l} \quad \text{A. 25}$$

$$\frac{\partial Dflux}{\partial l} = \sum_{j=1}^{2}\sum_{e}\sum_{l}\sum_{q} c_{p_j}\left[(\gamma - 1)l/\rho\right]_t Y_l C_{j_q} \vec{\nabla}\psi_q \cdot \vec{\nabla}\varphi_i M^e_{t,l} \quad \text{A. 26}$$

$$\frac{\partial Dflux}{\partial \varepsilon} = -\sum_{j=1}^{2}\sum_{e}\sum_{l}\sum_{q} c_{p_j}(\gamma - 1) Y_l C_{j_q} \vec{\nabla}\psi_q \cdot \vec{\nabla}\varphi_i M^e_{t,l} \quad \text{A. 27}$$